POLITECNICO DI TORINO
Repository ISTITUZIONALE

A coupled approach to model wear effect on shrouded bladed disk dynamics

Original
A coupled approach to model wear effect on shrouded bladed disk dynamics / Tamatam, L.R., Botto, D., Zucca, S.. - In: INTERNATIONAL JOURNAL OF MECHANICAL SCIENCES. - ISSN 0020-7403. - ELETTRONICO. - 237:(2023), p. 107816. [10.1016/j.ijmecsci.2022.107816]

Availability:
This version is available at: 11583/2973683 since: 2022-12-07T16:43:14Z

Publisher:
Elsevier

Published
DOI:10.1016/j.ijmecsci.2022.107816

Terms of use:

This article is made available under terms and conditions as specified in the corresponding bibliographic description in the repository

Publisher copyright
Elsevier postprint/Author's Accepted Manuscript

© 2023. This manuscript version is made available under the CC-BY-NC-ND 4.0 license
http://creativecommons.org/licenses/by-nc-nd/4.0/.The final authenticated version is available online at:
http://dx.doi.org/10.1016/j.ijmecsci.2022.107816

(Article begins on next page)

14 September 2026

https://doi.org/10.1016/j.ijmecsci.2022.107816

A coupled approach to model the effect of wear on the dynamics of shrouded bladed disks

Lakshminarayana Reddy Tamatam[1]*, Daniele Botto[1] *and* Stefano Zucca[1]

Abstract

This paper deals with modelling the effect of wear on the dynamics of the shrouded bladed disk with frictional contacts at the shrouds and the contact interface evolution. Prediction of fretting wear commonly occurring at the contacts of turbomachinery components, and its impact on the dynamics is increasingly researched due to the components subjected to their structural limits for performance and operating at high loading conditions. Over a lifetime, the fretting wear at these contacts could alter the global dynamic response of these bladed disks from the designed operating point and could lead to high vibration amplitudes. This study implements a coupled static/dynamic harmonic balance method (HBM) with wear energy approach and an adaptive wear logic to study the impact on the steady-state nonlinear dynamic response. Firstly, the methodology is applied to a cantilever beam with a contact patch and then to a shrouded bladed disk with shroud contacts using cyclic symmetry boundary conditions. The novelty of the paper is to show the effect of wear on the dynamics with the changing contact pre-load using a coupled approach. A wear acceleration parameter $\mathbf{v}_{w,max}$ is defined, and the impact of the choice of this parameter is discussed in detail on the computation time and the accuracy of results. The test cases demonstrate the impact of wear on the dynamic nonlinear response curves and the contact interface evolution for various scenarios.

Keywords: nonlinear structural dynamics, contact evolution, contact pre-load, fretting wear, harmonic balance method

[1] *Department of Mechanical and Aerospace Engineering,*

Politecnico di Torino, Corso Duca degli Abruzzi 24, 10129 Torino, Italy

** e-mail: lakshminarayana.tamatam@polito.it*

1. Introduction

Mechanical assemblies made of two or more components have contact interfaces between them. Relative sliding always occurs during operation, sometimes intentional for design and functional purposes and at times unintentional. In turbomachinery components, such as bladed disks, high modal density usually prevents out-of-resonance operation within the full operative range of the machine. As a consequence, to reduce resonant vibration amplitude, contacts interfaces are purposedly designed to dissipate energy by friction during vibration. The most common contact interfaces in bladed disks are blade root joints [1], ring dampers [2], underplatform dampers [3] and shrouds [4]. The drawback of contact interfaces that undergo small relative motion to provide friction damping is fretting wear, that changes the contact properties and parameters with a potential uncontrolled effect on the system dynamics and on the component life. The most relevant contact parameter for interfaces, designed to dissipate energy by friction, is the static pre-load, that keeps the bodies in contact, since its value strongly affects the contact stiffness and the amount of energy dissipated at the contact during periodic relative motions [5], thus affecting the system resonance frequency and its vibration amplitude.

In case of ring dampers, underplatform dampers and blade root joints, the static pre-load at the contact interfaces is due to the centrifugal force that acts on the ring, the damper and the blade respectively. In those cases, wear mostly affects the static pre-load distribution over the contact interfaces. In case of shrouds, the static pre-load is due partly to the centrifugal force, that twists the blade, and partly to the amount of static interlocking between adjacent blades at rest (typical of aero-engine applications). In both cases, as wear evolves in time, the mechanical interference at the shrouds between adjacent blades progressively reduces, affecting not only the distribution of the static pre-load over the contact interfaces but also its total amount. Asymptotically, as wear evolves, shrouded blades will tend towards a free-standing configuration without any coupling between adjacent blades. For the above-mentioned reasons, the need for a model and a method to track the effect of wear evolution on the dynamics of shrouded blades is even higher than for blades with other damping devices.

Wear ([6], [7]) is a multi-physics and multi-scale phenomenon caused by the micro-slip or gross tangential slip occurring at the contact interfaces. There is ample literature available on characterizing and predicting

fretting wear occurring at these contacts for various contact conditions ([8]–[14]). In particular, the effect of wear on the evolution of the dynamics of structures with friction contacts has been studied by Fantetti et al. [15], where the impact of wear on the dynamics of structures has been investigated experimentally and then validated using a constitutive numerical model - modified Bouc-Wen model. They studied the evolution of fretting wear and the dynamics during the running-in up to steady-state. They captured the evolution of fretting wear for a very short number of cycles up to a few millions of cycles. The study clearly showed the impact of the microscopic wear generated at the contact has on the resonant frequencies and damping and the corresponding change in dynamics in the running-in and steady-state conditions and it confirms the need for predictive modelling techniques able to track the evolution of the system dynamics as a consequence of wear evolution over the contact interfaces. Since friction contacts introduce nonlinearity to the system, nonlinear dynamic analysis are necessary and they can be performed either in time ([16], [17]) or frequency ([16], [18]–[24]) domain.

Direct Time Integration (DTI) provides the transient as well as steady-state response, but it is computationally demanding and it is not a feasible solution for practical scenarios and systems with a large number of degrees of freedom (DOF). On the other hand, the state-of-the-art frequency-domain method to compute the nonlinear response is the Harmonic Balance Method (HBM), that established itself as a standard in nonlinear forced response calculations due to its suitability for large systems and computational efficiency ([16], [18]–[23]). This method allows for lower solution times than DTI's, directly computing the steady-state response of the system, assuming a periodic response under periodic excitation. Krack and Gross's book [25] provides a detailed description of the method and examples of nonlinear vibration problems.

Today's need is embedding wear prediction tools into nonlinear dynamic solvers to study the impact of wear and contact interface evolution. There is little research available on this joint topic. Brake's book [26] provides an up-to-date comprehensive overview of the developments of mechanics of jointed structures so far. Some of the other notable researches are [15], [27]–[34]. Sfantos et al. ([8], [9]) have proposed the Boundary Element Method (BEM) techniques for wear simulation and optimization methods using incremental sliding BEM. Salles et al. ([30]–[32]) proposed DLFT and HBM techniques to compute the effect of wear on the dynamics of free-standing blades with blade root joints. They also further proposed a multi-scale method to predict the effect of fretting wear as the amount of wear in each fretting cycle is too small relative to the change in

dynamics. A multi-scale approach would work on two different time scales for wear and the dynamics. Armand et al. ([27], [28]) extended the previous work. They proposed a multi-scale approach in time and space to predict the effect of fretting wear on the dynamic response for bladed disks with underplatform dampers. Later, they also modelled the contact considering surface roughness and showed the change in the dynamic response of the system [29]. In the existing literature, no methods have been developed for shrouded blades.

The research, described in this paper, is a numerical work and aims at developing and implementing a method to predict the effect of wear on the dynamics of structures with contact interfaces and also the evolution of contact interface, using a static/dynamic coupled approach ([33], [35], [36]) developed for frequency domain nonlinear analysis of structures with friction contacts. The method is particularly suitable, although not limited to, shrouded blades. The need for a static/dynamic coupled approach in the calculation of nonlinear forced response levels of components with friction contacts has been demonstrated in ([37]), where experimental results could only be matched by numerical models, when the static and dynamic equilibria were solved simultaneously. Nonetheless, a static/dynamic coupled approach has never been implemented to predict the effect of wear on the nonlinear dynamics of structures with friction contacts.

In this paper, a wear model, based on the wear energy approach ([38]) is implemented in the static/dynamic coupled approach, thus allowing for the automatic update of the static pre-load distribution over the contact area during the nonlinear dynamic analysis, without any need for a separate static analysis, still necessary with the methods currently available in the literature. Two test cases are chosen to demonstrate the method – a cantilever beam with a contact patch and a shrouded bladed disk with shroud contacts and cyclic symmetry boundary conditions.

The novelty of this paper is two-fold:

1) Modelling the effect of wear on the nonlinear forced response of the system and the contact interface evolution by means of a static/dynamics coupled approach.

2) The impact of the choice of user-defined wear acceleration parameter $\mathbf{v}_{w,max}$ that is described in the paper.

2. Methodology

2.1 Governing equations of a generic system

The governing equation of motion of a generic system with contact interfaces is written as:

$$\mathbf{M}\ddot{\mathbf{Q}}(t) + \mathbf{C}\dot{\mathbf{Q}}(t) + \mathbf{K}\mathbf{Q}(t) = \mathbf{F}(t) + \mathbf{F}_c(\mathbf{Q}, \dot{\mathbf{Q}}, t) \tag{1}$$

where $\mathbf{M}, \mathbf{C}, \mathbf{K} \in \mathbb{R}^{N\times N}$ are the mass matrix, viscous damping matrix and stiffness matrix respectively; $\mathbf{Q}(t) \in \mathbb{R}^{N\times 1}$ is a nodal displacement vector; $\dot{\mathbf{Q}}$ is the time derivative of $\mathbf{Q}$; $\mathbf{F}(t) \in \mathbb{R}^{N\times 1}$ is the excitation force vector and $\mathbf{F}_c(\mathbf{Q}, \dot{\mathbf{Q}}, t) \in \mathbb{R}^{N\times 1}$ is the nonlinear contact force interaction vector. The components of the displacement vector $\mathbf{Q}$ is given by:

$$\mathbf{Q} = [\mathbf{q}_c{}^T \ \mathbf{q}_a{}^T \ \mathbf{q}_o{}^T]^T \tag{2}$$

where $\mathbf{q}_c$, $\mathbf{q}_a$ and $\mathbf{q}_0$ are the displacements of contact node DOFs, ~~accessory~~ actuation and readout (loading and response) node DOFs, and other node DOFs of the system respectively. $\mathbf{q}_a$ node DOFs include input and output node DOFs.

Since the contact DOF $\mathbf{q}_c$ and the ~~accessory~~ actuation and readout DOF $\mathbf{q}_a$ are usually much smaller in comparison to the other DOF $\mathbf{q}_o$, a reduction of the size of the nonlinear model is typically performed before computing the nonlinear solution. In this paper, the classical Craig-Bampton reduction method [39] is applied, retaining as physical coordinates the contact DOFs $\mathbf{q}_c$ and ~~accessory~~ actuation and readout DOFs $\mathbf{q}_a$ – cumulatively called as master nodes, and adding a certain number of fixed-interface modes $\boldsymbol{\eta}$.

$$\mathbf{q} = [\mathbf{q}_c{}^T \ \mathbf{q}_a{}^T \ \boldsymbol{\eta}^T]^T \tag{3}$$

where $\mathbf{q} \in \mathbb{R}^{n\times 1}$ and $n \ll N$. The equation (1) can be rewritten as:

$$\mathbf{m}\ddot{\mathbf{q}}(t) + \mathbf{c}\dot{\mathbf{q}}(t) + \mathbf{k}\mathbf{q}(t) = \mathbf{f}(t) + \mathbf{f}_c(\mathbf{q}, \dot{\mathbf{q}}, t) \tag{4}$$

where $\mathbf{m}, \mathbf{c}, \mathbf{k} \in \mathbb{R}^{n\times n}$ are the mass matrix, viscous damping matrix and stiffness matrix respectively; $\mathbf{q}(t) \in \mathbb{R}^{n\times 1}$ is a nodal displacement vector; $\mathbf{f}(t) \in \mathbb{R}^{n\times 1}$ is the excitation force vector; $\mathbf{f}_c(\mathbf{q}, \dot{\mathbf{q}}, t) \in \mathbb{R}^{n\times 1}$ is the nonlinear contact force interaction vector. These matrices and vectors are obtained after performing the Craig-Bampton reduction method. The system is unaffected by Craig Bampton reduction method as the reduction is

applied to internal linear DOFs excluding contact DOFs.

To solve the equation (4) for periodic excitation using HBM ([25]), the periodic quantities (i.e. displacements and forces) with an angular frequency of ω are expressed as truncated series of harmonic terms:

$$\boldsymbol{q}(t) = \Re\left(\sum_{h=0}^{H} \widehat{\boldsymbol{q}}^{(h)} e^{ih\omega t}\right);\ \boldsymbol{f}(t) = \Re\left(\sum_{h=0}^{H} \hat{\boldsymbol{f}}^{(h)} e^{ih\omega t}\right);\ \boldsymbol{f}_c(\boldsymbol{q}, \dot{\boldsymbol{q}}, t) = \Re\left(\sum_{h=0}^{H} \hat{\boldsymbol{f}}_c{}^{(h)}(\widehat{\boldsymbol{q}}) e^{ih\omega t}\right) \tag{5}$$

where $\Re(\cdot)$ represents the real part of the quantity.

By applying Galerkin's procedure with the multi-harmonic approximation, the time domain nonlinear differential equation (4) is transformed into a nonlinear algebraic equation with Fourier coefficients as defined in equation (5), and the balance equation is written as:

$$\boldsymbol{d}^{(h)}\widehat{\boldsymbol{q}}^{(h)} = \hat{\boldsymbol{f}}^{(h)} + \hat{\boldsymbol{f}}_c^{(h)}\ with\ h = 0..H \tag{6}$$

where $\boldsymbol{d}^{(h)} = (-(h\omega)^2\boldsymbol{m} + ih\omega\boldsymbol{c} + \boldsymbol{k})$ is the h^{th} dynamic stiffness matrix of the system. The equation (6) consists of the static ($h = 0$) and dynamic ($h = 1..H$) equations of the system coupled to each other by the Fourier coefficients of the nonlinear contact force $\hat{\boldsymbol{f}}_c$, that depend on the Fourier coefficients of the displacement $\widehat{\boldsymbol{q}}$. The number of harmonics H is chosen in a way to approximate the dynamics of the structure with sufficient accuracy. The residual equation is formulated by rewriting equation (6) as:

$$\boldsymbol{RES}^{(h)} = \boldsymbol{d}^{(h)}\widehat{\boldsymbol{q}}^{(h)} - \hat{\boldsymbol{f}}^{(h)} - \hat{\boldsymbol{f}}_c^{(h)}\ with\ h = 0..H \tag{7}$$

2.2 Governing equations of a shrouded bladed disk

Let us consider a shrouded bladed disk with shroud contact interfaces, as shown in Figure 1. The bladed disk is a tuned system because it is made of identical fundamental sectors arranged in a cyclical manner. Since the bladed disks are cyclic in nature, one can exploit the analysis by reducing the full bladed disk model to a single fundamental sector, by applying proper boundary conditions at the sector interfaces in the nonlinear dynamic analysis ([22], [40]).

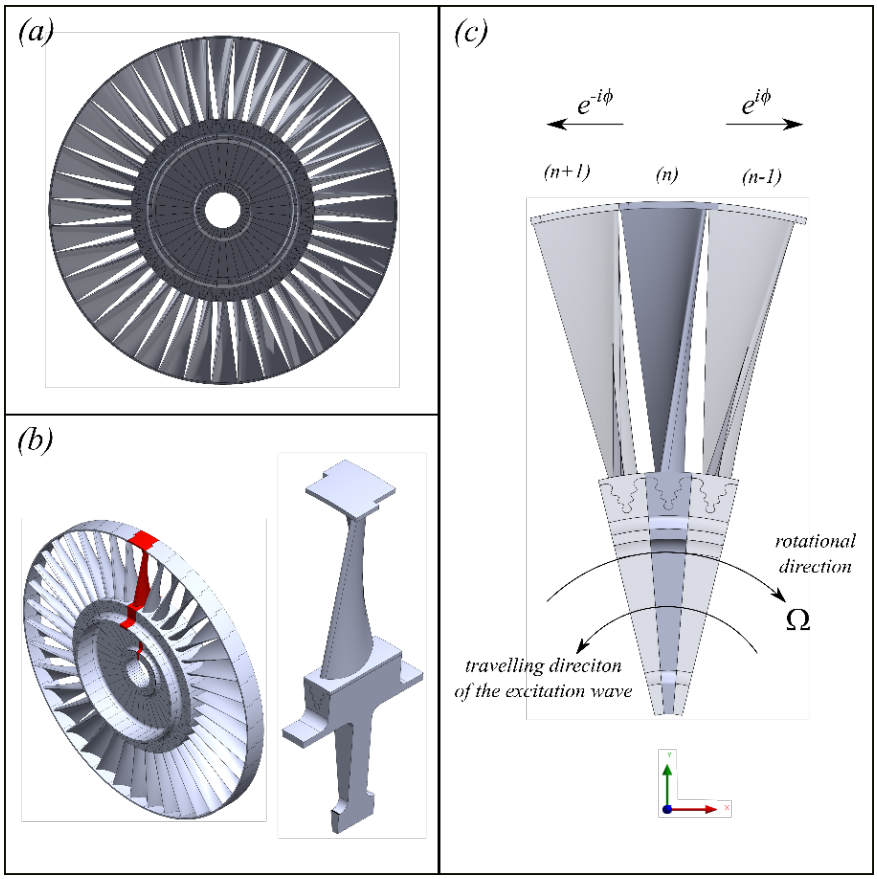

Figure 1: (a) Full bladed disk with shroud contacts (b) A fundamental blade-disk sector

(c) Schematic view of cyclic symmetry for bladed disk model

The equation of motion for a tuned bladed disk with contact interfaces with N_s sectors can be obtained by modifying equation (1) as:

$$\mathbf{M}^{(n)}\ddot{\mathbf{Q}}(t) + \mathbf{C}^{(n)}\dot{\mathbf{Q}}(t) + \mathbf{K}^{(n)}\mathbf{Q}(t) = {}^{(n)}\mathbf{F}(t) + {}^{(n)}\mathbf{F}_{c,l}\left(\Delta\mathbf{q}_{c,l}, \Delta\dot{\mathbf{q}}_{c,l}, t\right) + {}^{(n)}\mathbf{F}_{c,r}\left(\Delta\mathbf{q}_{c,r}, \Delta\dot{\mathbf{q}}_{c,r}, t\right) \quad (8)$$

where $n = 1..N_s$ is a sector number; $\mathbf{M}, \mathbf{C}, \mathbf{K} \in \mathbb{R}^{\mathrm{N}\times\mathrm{N}}$ denote the mass matrix, viscous damping matrix and the stiffness matrix respectively of n^{th} isolated bladed disk segment without cyclic boundary conditions; ${}^{(n)}\mathbf{Q}(t) \in \mathbb{R}^{\mathrm{N}\times 1}$ is a nodal displacement vector; ${}^{(n)}\mathbf{F}(t) \in \mathbb{R}^{\mathrm{N}\times 1}$ is the excitation force vector acting on n^{th} blade, and ${}^{(n)}\mathbf{F}_{c,l}, {}^{(n)}\mathbf{F}_{c,r} \in \mathbb{R}^{\mathrm{N}\times 1}$ are nonlinear contact force interaction vectors at the shrouds of the left and the right adjacent sectors respectively depending on the relative displacements and velocities. These contact forces depend in a nonlinear fashion on the relative displacements at the shroud contact.

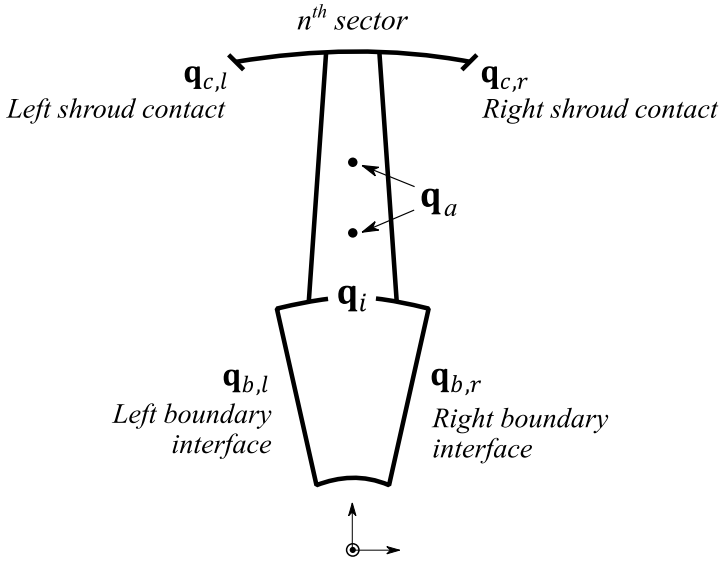

Figure 2: A schematic view of the isolated bladed disk segment

The displacement vector at n^{th} isolated bladed disk segment is written as:

$$ {}^{(n)}\mathbf{Q} = \left[{}^{(n)}\mathbf{q}_{b,l}{}^{T}\ {}^{(n)}\mathbf{q}_{b,r}{}^{T}\ {}^{(n)}\mathbf{q}_{a}{}^{T}\ {}^{(n)}\mathbf{q}_{c,l}{}^{T}\ {}^{(n)}\mathbf{q}_{c,r}{}^{T}\ {}^{(n)}\mathbf{q}_{i}{}^{T} \right]^{T} \tag{9} $$

where ${}^{(n)}\mathbf{q}_{b,l}$ and ${}^{(n)}\mathbf{q}_{b,r}$ are the nodal displacements of the left boundary segment interface and right boundary segment interface, respectively, as shown in Figure 2. ${}^{(n)}\mathbf{q}_{c,l}$ and ${}^{(n)}\mathbf{q}_{c,r}$ are the displacements of left and right shroud contact nodes, respectively. ${}^{(n)}\mathbf{q}_{a}$ are the nodes which contains the displacements of loading and response nodes, and ${}^{(n)}\mathbf{q}_{i}$ contains the displacements of other interior nodes of the system of the n^{th} segment.

Similar to the generic system, to solve the equation (8) for periodic excitation using HBM ([25]), the periodic quantities (i.e. displacements and forces) with an angular frequency of ω are expressed as truncated series of harmonic terms:

$$ \begin{gathered} {}^{(n)}\mathbf{Q}(t) = \Re\left(\sum_{h=0}^{H} {}^{(n)}\widehat{\mathbf{Q}}^{(h)} e^{ih\omega t} \right);\ {}^{(n)}\mathbf{F}(t) = \Re\left(\sum_{h=0}^{H} {}^{(n)}\widehat{\mathbf{F}}^{(h)} e^{ih\omega t} \right); \\ {}^{(n)}\mathbf{F}_{c,l}\left(\Delta\mathbf{q}_{c,l}, \Delta\dot{\mathbf{q}}_{c,l}, t\right) = \Re\left(\sum_{h=0}^{H} {}^{(n)}\widehat{\mathbf{F}}_{c,l}^{(h)} e^{ih\omega t} \right);\ {}^{(n)}\mathbf{F}_{c,r}\left(\Delta\mathbf{q}_{c,r}, \Delta\dot{\mathbf{q}}_{c,r}, t\right) = \Re\left(\sum_{h=0}^{H} {}^{(n)}\widehat{\mathbf{F}}_{c,r}^{(h)} e^{ih\omega t} \right) \end{gathered} \tag{10} $$

By applying Galerkin's procedure with the multi-harmonic approximation, the time domain nonlinear differential equation (8) is transformed into a nonlinear algebraic equation with Fourier coefficients as defined in equation (10), and the balance equation is written as:

$$\mathbf{D}^{(h)}\,{}^{(n)}\widehat{\mathbf{Q}}^{(h)} = {}^{(n)}\widehat{\mathbf{F}}^{(h)} + {}^{(n)}\widehat{\mathbf{F}}_{c,l}^{(h)} + {}^{(n)}\widehat{\mathbf{F}}_{c,r}^{(h)} \; with \; h = 0..H \tag{11}$$

where $\mathbf{D}^{(h)} = (-(h\omega)^2\mathbf{M} + ih\omega\mathbf{C} + \mathbf{K})$ is the h^{th} dynamic stiffness matrix of the system. The equation (11) consists of the static ($h = 0$) and dynamic ($h = 1..H$) equations of the system coupled to each other by Fourier coefficients of the nonlinear contact force ${}^{(n)}\widehat{\mathbf{F}}_{c,l}^{(h)}$ and ${}^{(n)}\widehat{\mathbf{F}}_{c,r}^{(h)}$ depending on the Fourier coefficients of the relative displacements and velocities. The number of harmonics H is chosen in a way to approximate the steady state dynamics of the structure with sufficient accuracy. The equation (11) has to be solved iteratively for the unknown displacement vector of n^{th} segment because of the nonlinear contact forces. Note the size of the dynamic stiffness matrix $\mathbf{D} \in \mathbb{C}^{(N(H+1)\times N(H+1))}$ and the force vectors ${}^{(n)}\widehat{\mathbf{F}}$, ${}^{(n)}\widehat{\mathbf{F}}_{c,l}$, ${}^{(n)}\widehat{\mathbf{F}}_{c,r} \in \mathbb{C}^{(N(H+1)\times 1)}$. The system of equations still refer to the single fundamental bladed disk sector. The cyclic symmetry boundary conditions will be implemented in the next steps.

2.3 Implementation of cyclic symmetry constraints

The turbine bladed disk is assumed to be subjected to a travelling wave type excitation, see ref. [22], [40] for detailed explanation. The inter-blade phase angle (IBPA) is defined as: $\emptyset = \frac{2\pi}{N}.EO$, where N is the number of blades and EO is the engine order that, in the Campbell diagram, crosses the resonance under investigation. Reducing the number of DOFs required for the nonlinear forced response analysis is done in two steps. First, the disk interface segment boundary DOFs are reduced using cyclic symmetry constraints and then similar constraints are applied to the shroud contact node DOFs.

Reducing the disk segment boundary DOFs using cyclic symmetry constraints:

Since the bladed disk is subjected to the travelling wave type excitation, it is assumed that the steady-state vibration response also represents a travelling wave. This results in a relationship between the right segment interface nodal DOF, and the left segment interface nodal DOF. Owing to the cyclic symmetry conditions based on the assumption of the turbine bladed disk is made of the similar bladed-disk fundamental sector, one

can write the following coupling relationship for the displacements at the segment boundary DOFs:

$$^{(n)}\widehat{\mathbf{q}}_{b,l}^{(h)} = {}^{(n)}\widehat{\mathbf{q}}_{b,r}^{(h)} e^{-ih\emptyset} \tag{12}$$

Redefining the reduced displacement vector of unknowns by considering the right-side boundary segment for h^{th} harmonic component and n^{th} sector as:

$$^{(n)}\widehat{\mathbf{Q}}^{(h)} = \widehat{\mathbf{T}}_{CS}{}^{(h)}\, {}^{(n)}_{red}\widehat{\mathbf{Q}}^{(h)} \tag{13}$$

Thereby making the new reduced displacement vector of unknowns as:

$${}^{(n)}_{red}\widehat{\mathbf{Q}}^{(h)} = \left[{}^{(n)}\widehat{\mathbf{q}}_{b,r}{}^{(h)^T}\ {}^{(n)}\widehat{\mathbf{q}}_{a}{}^{(h)^T}\ {}^{(n)}\widehat{\mathbf{q}}_{c,l}{}^{(h)^T}\ {}^{(n)}\widehat{\mathbf{q}}_{c,r}{}^{(h)^T}\ {}^{(n)}\widehat{\mathbf{q}}_{i}{}^{(h)^T} \right]^T \tag{14}$$

$$\widehat{\mathbf{T}}_{CS}{}^{(h)} = \begin{bmatrix} \mathbf{I}(e^{-ih\emptyset}) & 0 & 0 & 0 & 0 \\ \mathbf{I} & 0 & 0 & 0 & 0 \\ 0 & \mathbf{I} & 0 & 0 & 0 \\ 0 & 0 & \mathbf{I} & 0 & 0 \\ 0 & 0 & 0 & \mathbf{I} & 0 \\ 0 & 0 & 0 & 0 & \mathbf{I} \end{bmatrix} \tag{15}$$

Where $\widehat{\mathbf{T}}_{CS}{}^{(h)}$ is the cyclic symmetry constraint matrix for h^{th} harmonic component; $\mathbf{I}$ is the identity matrix of an appropriate size corresponding to the size of DOFs. Substituting the vector $^{(n)}\widehat{\mathbf{Q}}^{(h)}$ in equation (11) by the cyclic constraint relation as given in equation (13) for $h = 0..H$ and left-multiplying by the corresponding complex conjugate transpose of $\widehat{\mathbf{T}}_{CS}{}^{(h)}$ results in:

$$_{red}\widehat{\mathbf{D}}^{(h)}\ {}^{(n)}_{red}\widehat{\mathbf{Q}}^{(h)} = {}^{(n)}_{red}\widehat{\mathbf{F}}^{(h)} + {}^{(n)}_{red}\widehat{\mathbf{F}}^{(h)}_{c,l} + {}^{(n)}_{red}\widehat{\mathbf{F}}^{(h)}_{c,r}\ with\ h = 0..H \tag{16}$$

where $_{red}\widehat{\mathbf{D}}^{(h)} = \left(-(h\omega)^2\widehat{\mathbf{M}}^{(h)} + ih\omega\widehat{\mathbf{C}}^{(h)} + \widehat{\mathbf{K}}^{(h)}\right)$ is the h^{th} dynamic stiffness matrix of the system. Note that the complex mass matrix, viscous damping matrix and stiffness matrix ($\widehat{\mathbf{M}}, \widehat{\mathbf{C}}, \widehat{\mathbf{K}} \in \mathbb{C}^{(j(H+1)\times j(H+1))}$) are Hermitian because of the application of the cyclic symmetry constraints and ${}^{(n)}_{red}\widehat{\mathbf{F}}$, ${}^{(n)}_{red}\widehat{\mathbf{F}}_{c,l}$, ${}^{(n)}_{red}\widehat{\mathbf{F}}_{c,r} \in \mathbb{C}^{(j(H+1)\times 1)}$ where $j(H+1) < N(H+1)$ because of the successful elimination of the left boundary segment interface DOFs.

Reducing the shroud contact DOFs using cyclic symmetry constraints:

The displacement vector of unknowns can further be reduced by applying the cyclic symmetry constraints at the shroud contact DOFs and writing in relative displacement terms. Writing in relative displacements terms reduces the number of shroud contact DOFs by half as one can consider only the number of shroud contact DOFs of one side and reduce the size of the system required for nonlinear analysis. The relative displacement at the right-side shroud contact and the nonlinear contact force can be written as:

$$\begin{aligned} {}^{(n)}\Delta\hat{\mathbf{q}}_{c,r}^{(h)} &= {}^{(n)}\hat{\mathbf{q}}_{c,r}^{(h)} - {}^{(n-1)}\hat{\mathbf{q}}_{c,l}^{(h)} \\ {}^{(n)}\Delta\hat{\mathbf{q}}_{c,r}^{(h)} &= {}^{(n)}\hat{\mathbf{q}}_{c,r}^{(h)} - {}^{(n)}\hat{\mathbf{q}}_{c,l}^{(h)} e^{ih\emptyset} \\ {}^{(n)}\hat{\mathbf{f}}_{c,r}^{(h)} &= -{}^{(n)}\hat{\mathbf{f}}_{c,l}^{(h)} e^{ih\emptyset} \end{aligned} \tag{17}$$

The new displacement vector of unknowns in terms of relative displacements at the shroud contact becomes:

$${}^{(n)}_{rel}\hat{\mathbf{Q}}^{(h)} = \left[{}^{(n)}\hat{\mathbf{q}}_{b,r}{}^{(h)^T} \; {}^{(n)}\hat{\mathbf{q}}_{a}{}^{(h)^T} \; {}^{(n)}\Delta\hat{\mathbf{q}}_{c,r}{}^{(h)^T} \; {}^{(n)}\hat{\mathbf{q}}_{i}{}^{(h)^T} \right]^T \tag{18}$$

This leads to cutting down the shroud contact unknown DOFs by half by considering either right or left contact, hence reducing the size of the nonlinear computation. Similarly, a relative displacement cyclic symmetry transformation matrix [41] can be defined, and the balance equation (16) can be rewritten as:

$${}_{rel}\hat{\mathbf{D}}^{(h)}\,{}^{(n)}_{rel}\hat{\mathbf{Q}}^{(h)} = {}^{(n)}_{rel}\hat{\mathbf{F}}^{(h)} + {}^{(n)}_{rel}\hat{\mathbf{F}}^{(h)}_{c,r} \; with \; h = 0..H \tag{19}$$

where $\hat{\mathbf{M}}, \hat{\mathbf{C}}, \hat{\mathbf{K}} \in \mathbb{C}^{(k(H+1)\times k(H+1))}$ and ${}^{(n)}_{rel}\hat{\mathbf{F}}$, ${}^{(n)}_{rel}\hat{\mathbf{F}}_{c,r} \in \mathbb{C}^{(k(H+1)\times 1)}$ where $k(H+1) < j(H+1)$.

Since the number of shroud contact nodes, boundary nodes, ~~accessory~~ actuation and readout nodes DOFs are much smaller than the number of internal DOFs, as described for the generic system, the classical Craig-Bampton reduction method [39] is applied, retaining as physical coordinates the right segment interface nodes, right shroud contact nodes, actuation and readout ~~accessory~~ nodes DOFs – collectively called as master nodes, and adding a certain number of fixed-interface modes $\boldsymbol{\eta}$.

$${}^{(n)}\hat{\mathbf{q}}^{(h)} = \left[{}^{(n)}\hat{\mathbf{q}}_{b,r}{}^{(h)^T} \; {}^{(n)}\hat{\mathbf{q}}_{a}{}^{(h)^T} \; {}^{(n)}\Delta\hat{\mathbf{q}}_{c,r}{}^{(h)^T} \; {}^{(n)}\boldsymbol{\eta}^T \right]^T \tag{20}$$

where ${}^{(n)}\hat{\mathbf{q}} \in \mathbb{C}^{m(H+1)\times 1}$ and $m(H+1) \ll k(H+1)$. Finally, the equation (19) can be reformulated using equation (20) as:

$$\hat{\mathbf{d}}^{(h)\,(n)}\hat{\mathbf{q}}^{(h)} = {}^{(n)}\hat{\mathbf{f}}^{(h)} + {}^{(n)}\hat{\mathbf{f}}_{c,r}^{(h)} \; with \; h = 0..H \tag{21}$$

By rearranging equation (21), the residual equation is written as:

$$\mathbf{RES}^{(h)} = \hat{\mathbf{d}}^{(h)\,(n)}\hat{\mathbf{q}}^{(h)} - {}^{(n)}\hat{\mathbf{f}}^{(h)} - {}^{(n)}\hat{\mathbf{f}}_{c,r}^{(h)} \; with \; h = 0..H \tag{22}$$

To use the nonlinear solvers, the residual has to be supplied in the real form. Hence, the complex form residual equation (7) and equation (22) is split into its real and imaginary components to real form to minimize the residual to an acceptable tolerance and find the unknown displacement vector as:

$$\mathbf{RES} = \left[\mathbf{RES}^{(0)}, \Re\left(\mathbf{RES}^{(1)}\right), \Im\left(\mathbf{RES}^{(1)}\right) \ldots \Re\left(\mathbf{RES}^{(H)}\right), \Im\left(\mathbf{RES}^{(H)}\right)\right]^{\mathrm{T}} \tag{23}$$

2.4 Contact Model

The solution of the balance equations requires the contact forces to be computed at each iteration from the relative displacements at the contacts and a contact model is necessary for this purpose. There are various node-to-node and patch-to-patch contact models available in the literature ([42]–[54]) such as Coulomb slider, Jenkins element – 2D and 3D with constant and variable normal load, Iwan model and its variations, Bouc-Wen model, Valanis model, LuGre model, etc.

In our study, we chose the state-of-the-art node-to-node 2D Jenkins element with a variable normal load to compute the contact forces, as shown in Figure 3(a). A typical hysteresis loop of the tangential contact force vs the tangential relative displacement is shown in Figure 3(b). The contact element is characterized by two linear springs in the tangential and normal direction with tangential (k_t) and normal (k_n) contact stiffness, at each node pair over the contact interface. The contact model allows to characterize and simulate three possible contact states – stick, slip and separation.

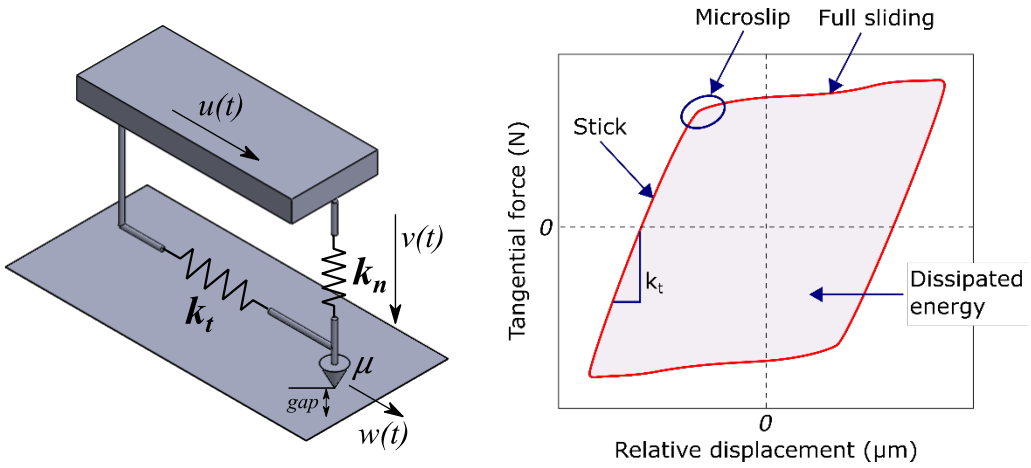

Figure 3: (a) Jenkin's element contact model with variable normal load, (b) A typical hysteresis loop

At each element, the contact forces – tangential force $T(t)$ and the normal force $N(t)$ depend on the relative tangential and normal displacements of the corresponding node pair, namely $\mathbf{u}(t)$ and $\mathbf{v}(t)$ respectively [35]. The friction limit value is defined by the Coulomb law as $\mu N(t)$, where μ is the coefficient of friction. To consider the friction phenomena occurring at the interface in the tangential direction, a slider is used to connect the two bodies. When the tangential force exceeds the limit value, the slider starts moving, and the amount of slip between the nodes is $\mathbf{w}(t)$.

Since the contact is a unilateral constraint, the normal contact force $N(t)$ is defined at each time t as:

$$N(t) = \max(k_n \mathbf{v}(t), 0) \tag{24}$$

When $\mathbf{v}(t)$ is negative, no normal contact force is allowed, and separation occurs, hence referred to as separation state.

For the tangential direction, the tangential contact force $T(t)$ is dependent on the contact state as defined by:

$$T(t) = \begin{cases} k_t\{\mathbf{u}(t) - \mathbf{w}(t)\} & stick\ state \\ \mu N(t) sign(\dot{\mathbf{w}}) & slip\ state \\ 0 & lift-off\ state \end{cases} \tag{25}$$

The contact forces are computed using predictor-corrector logic [22]. At each time t a predictor step is performed assuming the stick contact conditions:

$$T^p(t) = k_t[\mathbf{u}(t) - \mathbf{w}(t)] = k_t[\mathbf{u}(t) - \mathbf{w}(t - \Delta t)] \tag{26}$$

Where Δt is the time step, then a corrector step is performed to compute the actual value of $T(t)$ given by:

$$T(t) = \begin{cases} T^p(t) & stick\ state \\ \mu N(t) sign\left(T^p(t)\right) & slip\ state \\ 0 & lift-off\ state \end{cases} \tag{27}$$

Each cycle in time domain is discretized with 2e8 time steps. The slider displacement $\mathbf{w}(t)$ is computed as:

$$\mathbf{w}(t) = \begin{cases} \mathbf{w}(t-\Delta t) & stick\ state \\ \mathbf{u}(t) - \mu N(t) sign\left(T(t)\right)/k_t & slip\ state \\ \mathbf{u}(t) & lift-off\ state \end{cases} \tag{28}$$

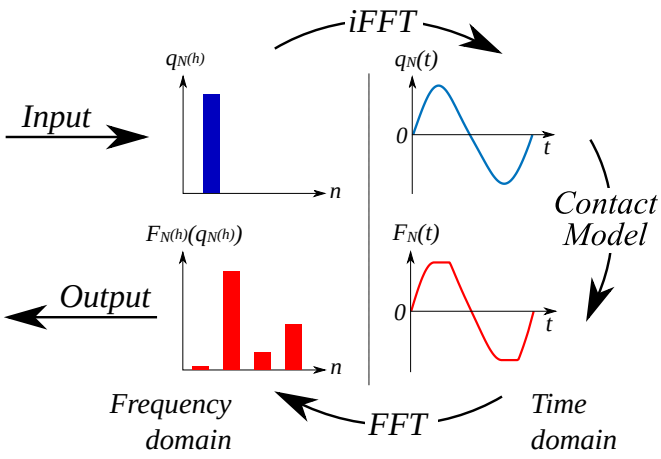

Figure 4: Alternating Frequency Time (AFT) method

2.5 Solution process

The balance equations are solved in the frequency domain using the HBM, whereas the contact forces are computed in the time domain. Hence an Alternate Frequency/Time (AFT) method ([55], [56]) is employed. The periodic relative displacements are converted from the frequency domain to the time domain by applying Inverse Fast Fourier Transform and then run through the contact model. The periodic contact forces are obtained in the time domain. Then applying Fast Fourier Transform is applied to obtain the Fourier coefficients of contact forces, as shown in Figure 4.

Newton-Raphson logic is implemented for the iterative solution process of the balance equations in the frequency domain. The Jacobian matrix needed to perform the generic iteration is computationally expensive if using MATLAB built-in finite difference method (FDM) for large systems. Hence an analytical Jacobian is implemented based on the works of [22], [57], highly increasing the speed of the solution by many folds. The computation of contact forces, necessary for an accurate forced response prediction, require accurate values of

the normal and tangential contact stiffness. The closed-form solutions needed to compute the global tangential (k_t) and normal (k_n) contact stiffness are based on the analytical equations available in the literature ([58]–[61]). Then the contact stiffnesses are distributed over the contact area according to the individual elemental contribution.

2.6 Wear computation

To predict the effect of fretting wear on the forced response of a bladed disk, wear has to be evaluated. There are many wear models [62] available in the literature, such as Archard's law [7], wear energy approach [38], thermodynamics approach, etc. Due to its simple nature in the formulation, good correlation with experiments ([11], [12], [63]), lower computation effort and easy implementation in the forced response solvers to evaluate the nonlinear dynamics, a wear energy approach is used. Initially, the dynamic forced response is computed with pristine contact surfaces without any wear. The nodal wear depth $\mathbf{v}_w$ is defined as:

$$\mathbf{v}_w = Z_W \frac{\alpha E}{A} \tag{29}$$

where A is the area associated with the node pair, α is the wear coefficient for a particular contact pair, and E is the energy dissipated over one cycle. It is worth mentioning that A depends on the finite element mesh over the contact surface, while α is the experimentally obtained parameter for a specific material couple ([64]–[66]) and E is obtained by evaluating the area inside the hysteresis loop of the tangential contact force versus the tangential relative motion of the bodies in contact. The control parameter of equation (29) is Z_W – number of cycles.

The process of updating the contact surface due to wear after one cycle is called a wear iteration. With materials typical of turbine blades, the wear depth obtained at each vibration cycle is so small that no significant effect on the forced response of the system is observed if a wear iteration is performed at each vibration cycle. Hence, a wear acceleration technique is used, where the wear depth $\mathbf{v}_w$ associated at each node pair is considered for Z_W number of cycles.

In this paper, an adaptive strategy is used, and the value of Z_W at each wear iteration is computed as:

$$Z_W = floor\left(\frac{\mathbf{v}_{w,max}}{max(\Delta h_{ij})}\right) \tag{30}$$

where, $\mathbf{v}_{w,max}$ is a user-defined parameter and Δh_{ij} is the nodal wear depth at the contact patch for one vibration cycle. Choosing $\mathbf{v}_{w,max}$ is empirical at this stage, as there are no guidelines from the experiments what value is most suitable in terms of accuracy of results. However, we present a few thumb rules one can use to define the parameter $\mathbf{v}_{w,max}$:

- the maximum wear depth allowed for each wear iteration, directly selected by the user

  For example, let us consider an assembly with a contact interface is functional up to a contact wear depth of 100 µm. In this case, the user can arbitrarily discretize this maximum allowable wear depth into 100 parts and define $\mathbf{v}_{w,max}$ as 1 µm. By doing this, the user can visualise the contact evolution and the effect on the nonlinear response plots at sufficient intervals before the functional failure of the assembly.

- the percentage of the maximum static deflection for the given static loads acting at the contact

  This method is more quantitative than the previous arbitrary method. $\mathbf{v}_{w,max}$ is a parameter of the static loading condition in the absence of the contact (free condition). The thought process is when there is complete separation due to eventual wear loss as in the case of shroud contacts under extreme wear, the bladed disk behaves under open contact condition at the shrouds acting as a free standing cantilever beam. Irrespective of the geometry, size and loading scenario of the system, $\mathbf{v}_{w,max}$ can be defined as a percentage of the maximum static deflection at the contact. For example, $\mathbf{v}_{w,max}$ can be chosen as 0.1% to 10% of the maximum static deflection (δ_{max}).

- the maximum tolerable error in wear depth

  This is more of a special case. Let us consider that the user has a very strict requirement of the accuracy of wear depth needed in each wear iteration. Then $\mathbf{v}_{w,max}$ can be defined directly as the value of this wear depth.

In this study, we define $\mathbf{v}_{w,max}$ as the percentage of the maximum static deflection at the contact patch for the given static loading condition under open condition. This percentage is varied between 0.5% to 10% of the maximum static deflection (δ_{max}). This parameter determines Z_W, in turn, is a trade-off between the accuracy of the results and computation time needed. A low value of Z_W will allow for a more accurate, but more time-consuming analysis, the opposite will happen if a high value of Z_W is selected.

Once the term $\mathbf{v}_w$ is computed using equation (29), the wear iteration is performed by updating the 0^{th} order Fourier coefficient of the normal relative displacement at the contact in the following way:

$$\mathbf{v}(t) = \sum_{h=0}^{H} \hat{\mathbf{v}}^{(h)} e^{ih\omega t} - \mathbf{v}_w \tag{31}$$

After the wear iteration, the forced response of the updated system is computed by solving the updated balance equations, taking into account the effect of the wear depth on the static pre-load and the nonlinear dynamics of the system simultaneously.

It is here worth mentioning that equation (31) allows for a direct update of the governing equations of the system since the static term (h = 0) is included in the set of nonlinear equations to solve. This method allows computing the effect of wear on the forced response with 'changing pre-load' without the need for a separate nonlinear static analysis routine to compute the contact pre-load distribution.

The results are shown and discussed in the next section. Figure 5 gives an overview of the steps with pre-processing and solution phase to compute the effect of wear on the nonlinear dynamic response. The pre-processing can be done using any standard commercial software. In this study, ANSYS is used to generate the FE model, perform CB-CMS and to extract the reduced Mass and Stiffness matrices. For the solution phase and post-processing the results MATLAB is used.

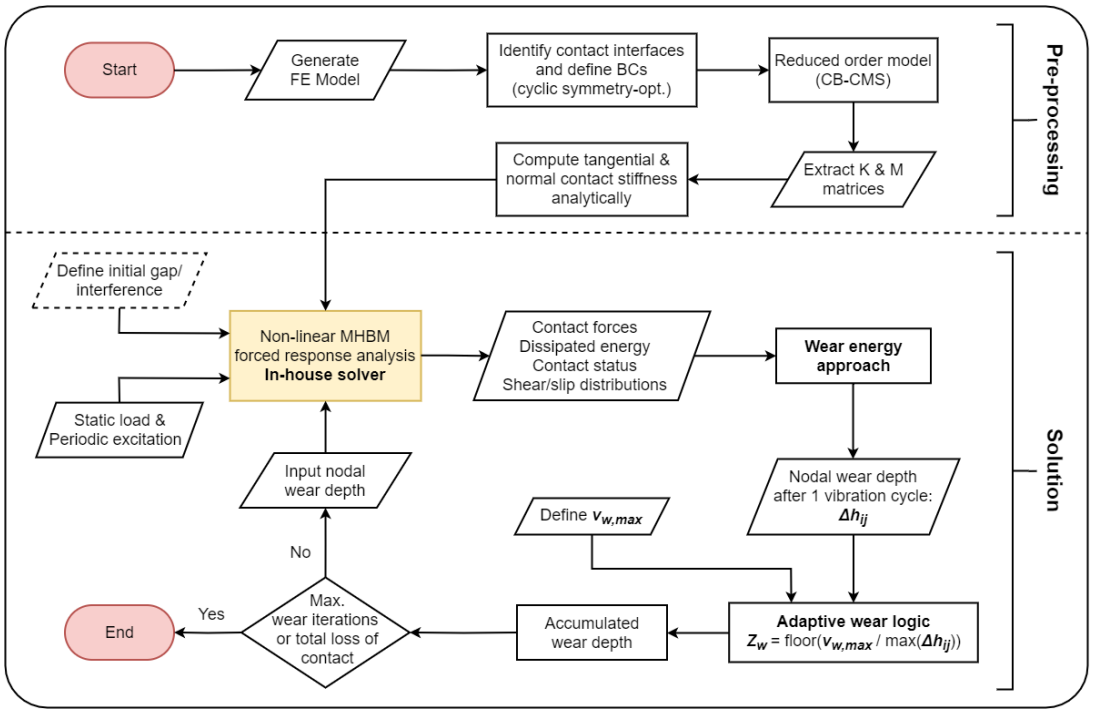

Figure 5: Flowchart showing an overview of steps to obtain the nonlinear dynamic response with wear

3. Test Case – description, results and discussion

The main test case here is the tuned shrouded bladed disk with shroud contacts with cyclic symmetry boundary conditions. Before jumping on to the test case, the proposed method is first evaluated on a simple cantilever beam with a contact patch on one side and clamped at the other end. The two test cases demonstrate the proposed methodology with changing pre-load and the contact surface evolution during wear. The goal for the test cases is to choose the static load and the excitation in such a way that there is accelerated wear and total loss of contact due to wear with high energy dissipation at each cycle. This will aid validation in terms of the number of wear iterations, wear profile evolution and correlate the wear profile with the analytical free case. Also, the effect of the choice of parameter $\mathbf{v}_{w,max}$ is quantified in terms of accuracy and computational demand. In the following test cases, $\mathbf{v}_{w,max}$ is defined as a percentage of maximum static deflection under static loading conditions. Hence, a preliminary static analysis is performed to compute the maximum static deflection as if the contact was open without the presence of the second body.

3.1 Test Case 1: Cantilever beam

A steel cantilever beam with a contact patch and loading conditions as shown in Figure 6(a) and (b) and Table 1 is chosen as a test case to demonstrate the impact of wear on the dynamic response. The FE model mesh is shown in Figure 6(c). The contact elements at the contact patch are connected as node-to-node pair to the ground with the 2D Jenkins element contact model with the variable normal load, as shown in Figure 6(d). The beam is loaded at the mid-section so that as the wear progresses, the contact pre-load and the contact zone changes considerably. The contact patch is made up of 169 node pairs, and the grid distribution is as shown in Figure 7 with a response node as the centre node of the contact patch. Maximum static deflection (δ_{max}) in this case is considered as the maximum deflection at the contact patch for the applied static load under open condition, as shown in Table 1.

Table 1: Parameters for the Cantilever beam and the contact patch

Parameter	**Value**
Material	Steel
Young's modulus (E)	210 GPa
Density (ρ)	7860 kg/m^3
Beam dimension	200mm L x 20 mm H x 20mm D
Contact patch dimension	20mm x 20mm
No. of contact elements	169
Tangential contact stiffness (k_t)	470 N/µm
Normal contact stiffness (k_n)	583 N/µm
Friction coefficient (μ)	0.5
Wear energy coefficient (α)	2e3 µm^3/J
Static load (F_{static})	20 kN
Static load/Excitation ratio (F_{static} / F_{ex})	2
Choice of $\mathbf{v}_{w,max}$	{0.5%, 1%, 2%, 5%, 10%} of δ_{max}

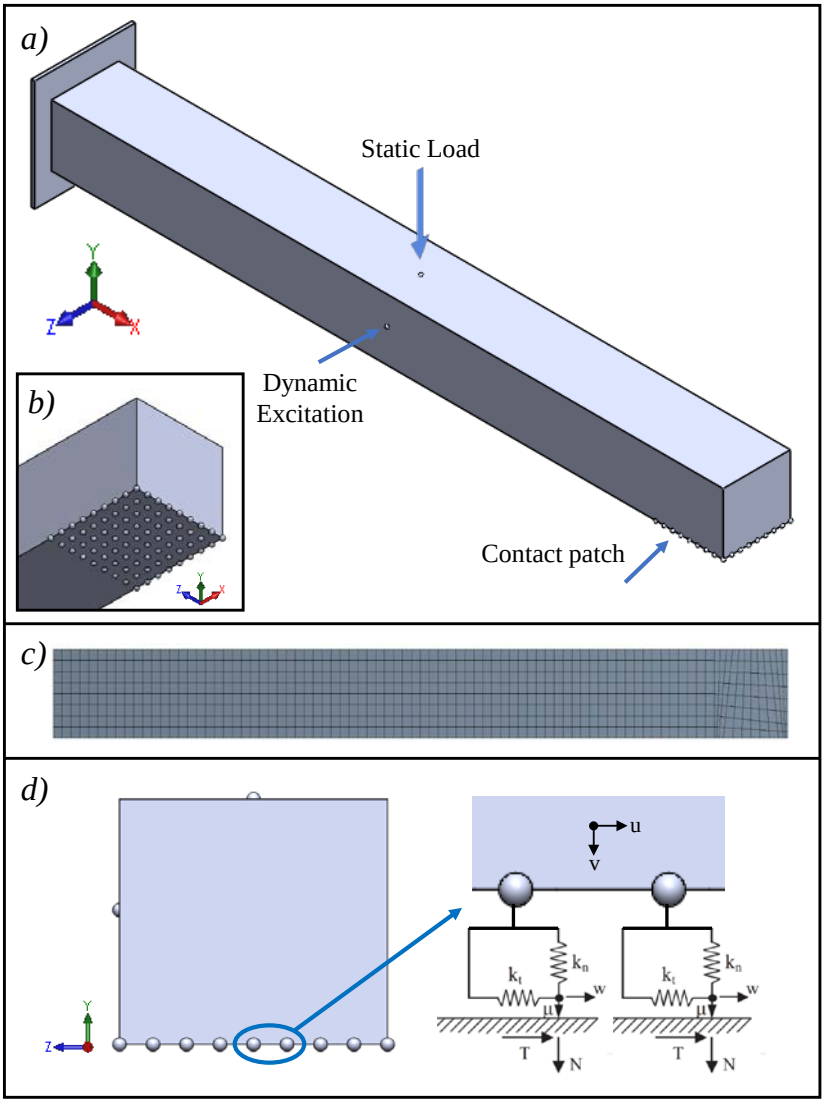

Figure 6: (a) 3D Model of a cantilever beam, (b) a close-up view of the contact patch, (c) FE mesh of the beam and (d) contact elements connection

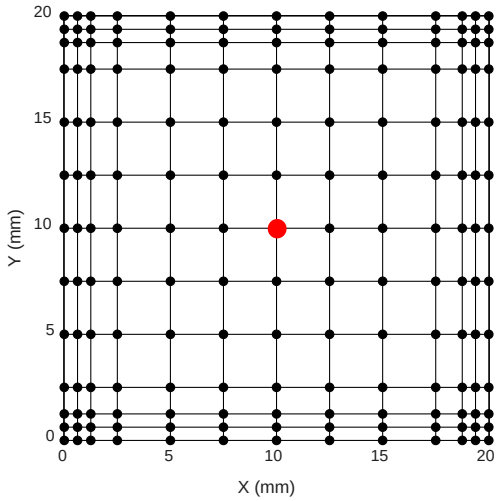

Figure 7: Contact patch with 169 elements and the centre response node (red dot)

The beam is excited by a harmonic transverse force, as shown in Figure 8, while the contact pre-load is provided by a vertical static load. Figure 8 also shows the static deflection and the shape at the initial contact condition with the second body and at the free condition when the second body is absent.

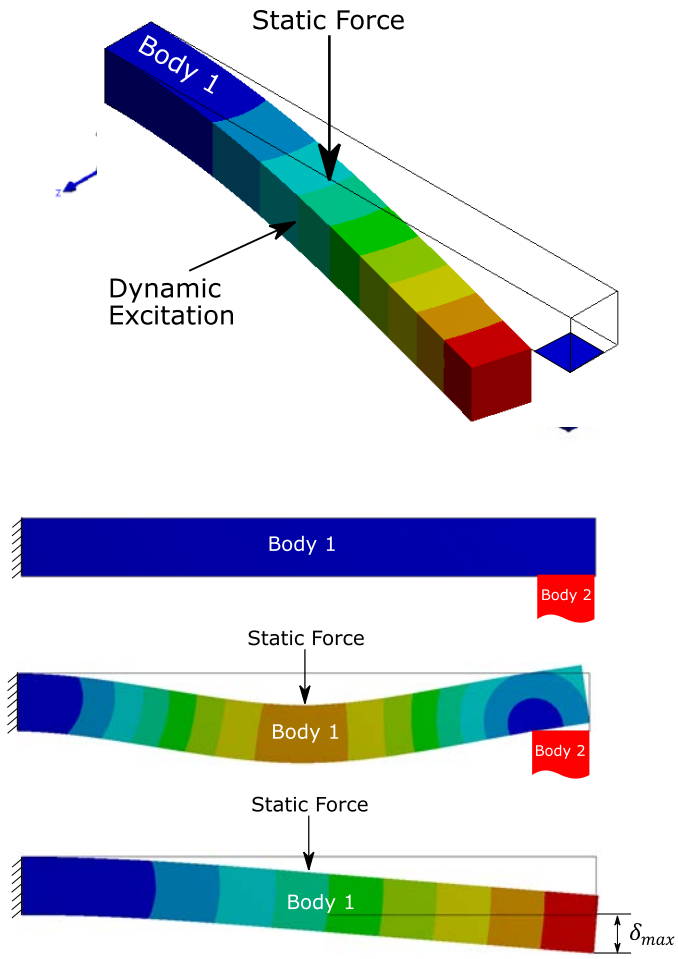

Figure 8: Excitation mode (first bending mode at 406 Hz) (top) and highlighting static deflection state with and without body 2 (bottom)

The FE model is generated using ANSYS, and the contact interface and boundary conditions are identified and defined in ANSYS. A Craig-Bampton Component Mode Synthesis (CB-CMS) [39] is performed by defining contact patch nodes and loading nodes as master nodes and retaining first 15 fixed interface modes to reduce the size of the system needed for the nonlinear dynamic analysis. Otherwise, the dynamic analysis with all DOFs would be large and prohibitively time-consuming. Reduced mass and stiffness matrices are extracted after the reduction process. The reduced system has 534 DOFs. The solution algorithm is followed, as shown in Figure 5. 0^{th} and 1^{st} order harmonics are used to solve the static and dynamic balance equations in the frequency domain using HBM. Analytically computed tangential and normal contact stiffness is computed,

taking into account the dimensions of the contact patch. These stiffnesses, which are assumed constant throughout the simulation, are distributed over the contact patch according to the elemental area contribution. If necessary, for future simulations, the friction co-efficient and contact stiffnesses can be used as a variable with respect to the energy dissipation if deemed for certain material behaviour and loading conditions.

A preliminary linear analysis is performed to obtain free and stick states of the contact, and the responses at these states are assumed as reference. The computed nonlinear response can then be compared with these two reference states. An initial gap/interference, if any, can also be defined using the current algorithm by offsetting in the direction normal to the contact. In the present case, the gap is set to 0 as the beam is resting on top of the body 2 before the static forces are applied to the system. Then both static and periodic forces are applied at the indicated excitation nodes. The contact forces, dissipated energy, contact status of each node and the shear/slip distributions are computed by solving equation (6). The wear energy approach, described in Section 2.6, is implemented to calculate the nodal wear depth at the contact patch for one vibration cycle. As the nodal wear depth is so minuscule at each vibration cycle, the dynamics is hardly affected. An adaptive wear acceleration logic is implemented by defining a parameter $\mathbf{v}_{w,max}$ as described in the previous section. The parameter $\mathbf{v}_{w,max}$ reduces the number of wear iterations, thus reducing the computation time, compared to running dynamic analysis for each vibration cycle. Since $\mathbf{v}_{w,max}$ is a user-defined value, the effect of the choice of $\mathbf{v}_{w,max}$ is also quantified. The iterative loop is performed until the required number of vibration cycles are obtained or until the complete loss of contact. Figure 9 shows the fineness of cumulative wear depth plots at the contact patch for different values of $\mathbf{v}_{w,max}$.

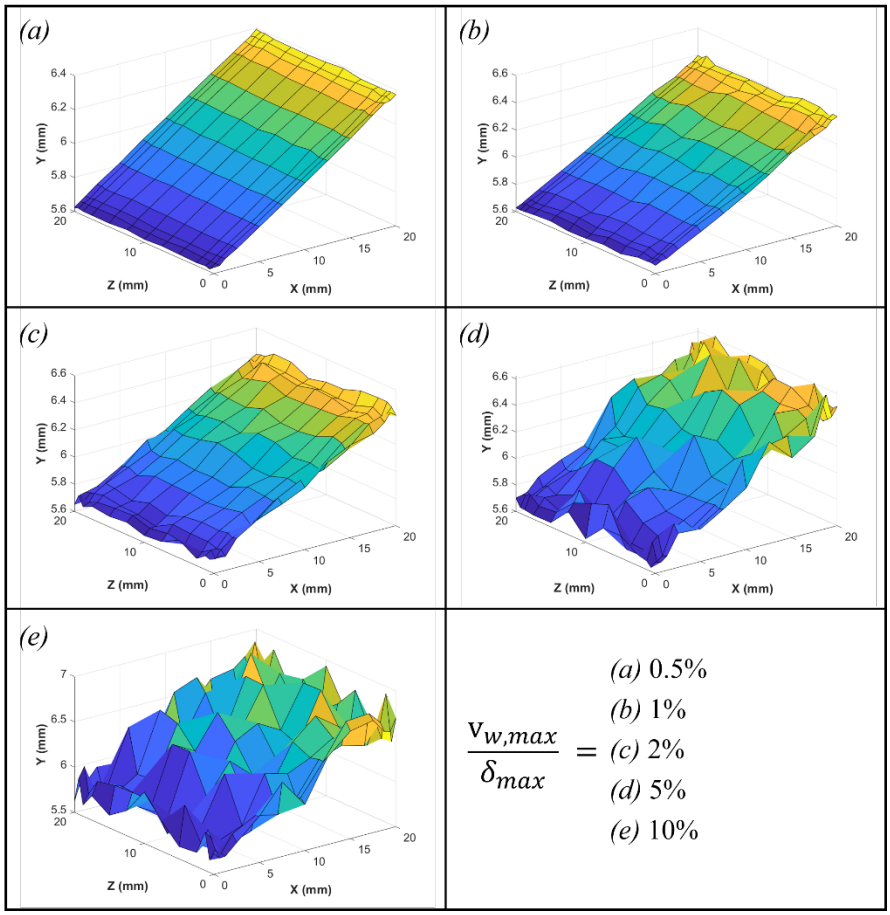

Figure 9: Cumulative wear depth plots at the contact patch for complete loss of contact for different values of $\mathbf{v}_{w,max}/\boldsymbol{\delta}_{max}$

Figure 10 shows the response curves of reference free and stick state along with the backbone curve of the maximum amplitude of response at each wear iteration for $\mathbf{v}_{w,max}$ = 5% of δ_{max}. It is evident and logical that, as the wear progresses, the contact interface loosens, and the contact tends towards the free state. The current formulation automatically takes into consideration the changing pre-load and is reflected in the response plots. Figure 11 provides an insight into the physical state of the system, cumulative wear depth and the contact status at different wear iterations. The wear iterations are chosen at the beginning, intermediate and at the end of the wear just before the complete loss of contact.

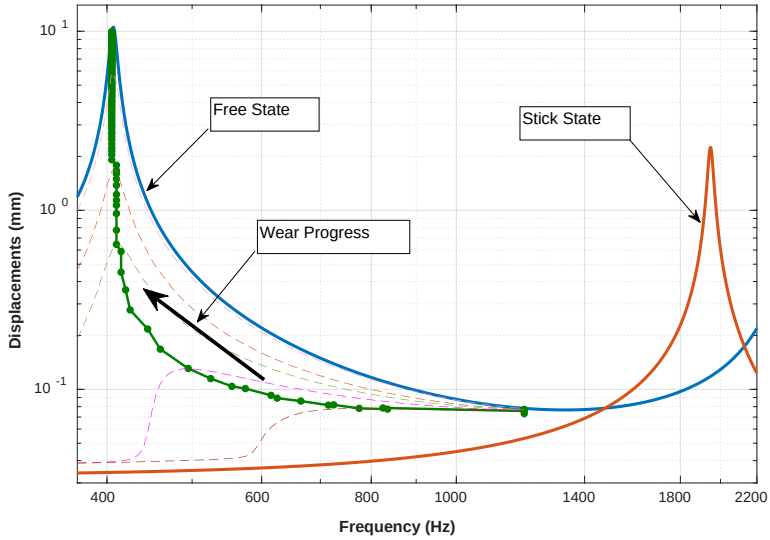

Figure 10: Response plot showing the backbone of the nonlinear response obtained as wear progresses around first bending mode with reference free and stick states for $\mathbf{v}_{w,max}$ = 5% of $\boldsymbol{\delta}_{max}$

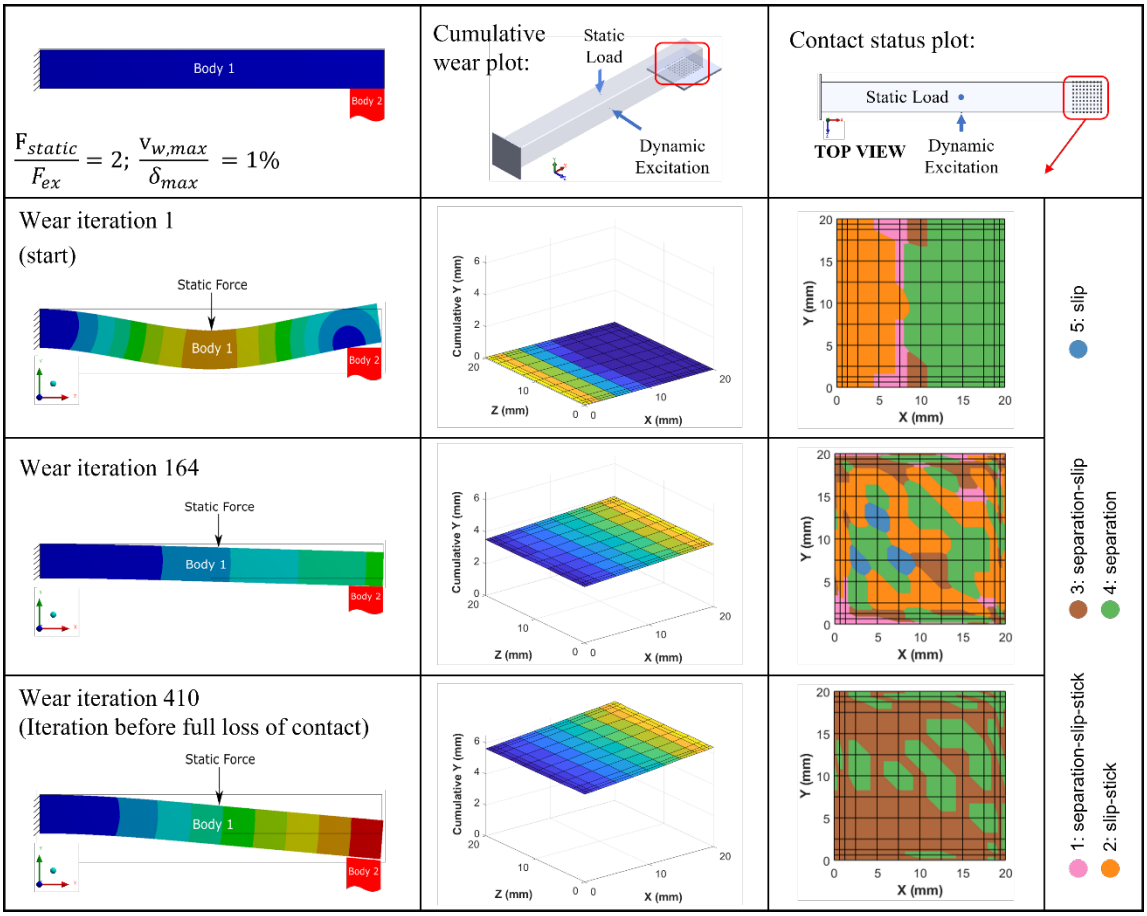

Figure 11: A result matrix showing - starting, intermediate and ending wear iteration just before the full loss of contact for the given test case highlighting the beam physical state, cumulative wear depth until that particular wear iteration and the contact status at that wear iteration

Figure 12 shows the plot of the number of vibration cycles at each wear iteration versus the number of wear iterations. For the shown plot, it took 183 wear iterations with the choice of $\mathbf{v}_{w,max}$ = 5% of δ_{max}. In other words, with the allowed wear depth of 5% of maximum static deflection at each wear iteration, it took 183 wear iterations to completely lose the contact with the second body. Depending on the loading configuration, the shape of this graph can be different. In this example, as shown in Figure 11 of wear iteration 1, the contact started with a line contact at the inner edge of the contact between the body 1 and body 2, and proceeded to establish an area contact with an increase in wear iterations. The close-up of the contact state at the beginning and at the end, is also shown in Figure 12. The criteria to complete one wear iteration is the amount of wear depth achieved, which is predetermined by the user input. At the start of the wear and towards the end, a relatively high number of cycles are needed to achieve this limit of wear depth to satisfy the wear iteration because of partial contact. However, when the contact is fully engaged, lower number of cycles can satisfy the wear depth criteria because of large contact, hence more energy dissipation.

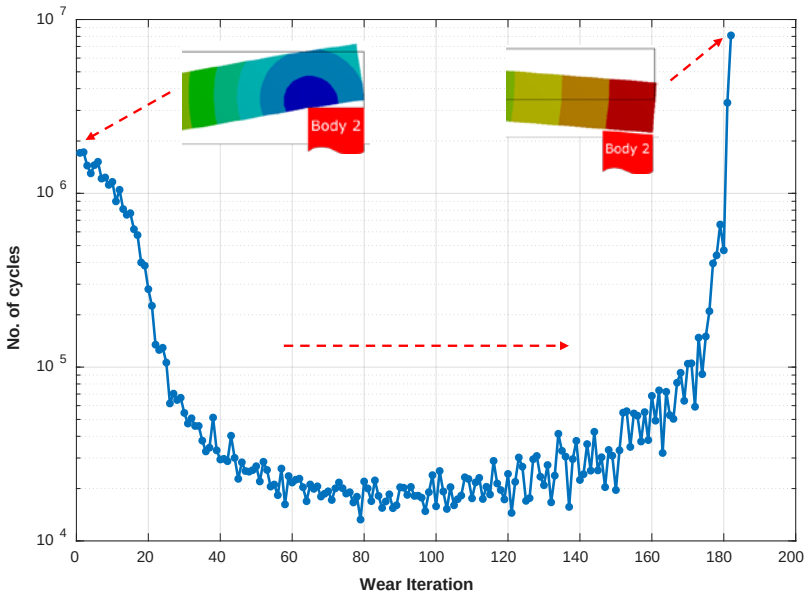

Figure 12: Wear iteration versus the number of vibration cycles plot showing the trend as the wear progresses from the start state to the complete loss of contact for $\mathbf{v}_{w,max}$ = 5% of $\boldsymbol{\delta_{max}}$

[Note: the number of cycles is adaptive at each wear iteration]

Figure 13 shows the maximum response amplitude at a particular wear iteration versus the cumulative number of cycles. It is evident the effect of $\mathbf{v}_{w,max}$ on the number of cycles at which the maximum response starts increasing. The accuracy of the proposed method for different values of $v_{w,max}$ is here investigated, by using

as a reference the analysis performed with $\mathbf{v}_{w,max}/\delta_{max}$ = 0.5%, since no significant effects was observed by further reducing the value of $v_{w,max}$. Ideally, the best benchmark would be the response computed with Z_W = 1 (one wear iteration per vibration cycle), but it is prohibitively time-consuming. It is clear that the choice of $\mathbf{v}_{w,max}$ is the trade-off between the computational cost and the accuracy of results; the lower the value of $\mathbf{v}_{w,max}$, the smoother the wear evolution and the contact patch wear profile is, due to the higher number of wear iterations. In general, a reasonable strategy should be based on a convergence analysis of the response as the value of Z_W is progressively reduced. In this particular case, for relatively high values of $\mathbf{v}_{w,max}$ (from 2% to 10% of δ_{max}) the analysis predicts the rapid increase in maximum response to occur earlier than the benchmark. Interestingly, when $\mathbf{v}_{w,max}/\delta_{max}$ = 1%, opposite results are obtained, showing that non-monotonic trend of the response during a convergence analysis can be observed.

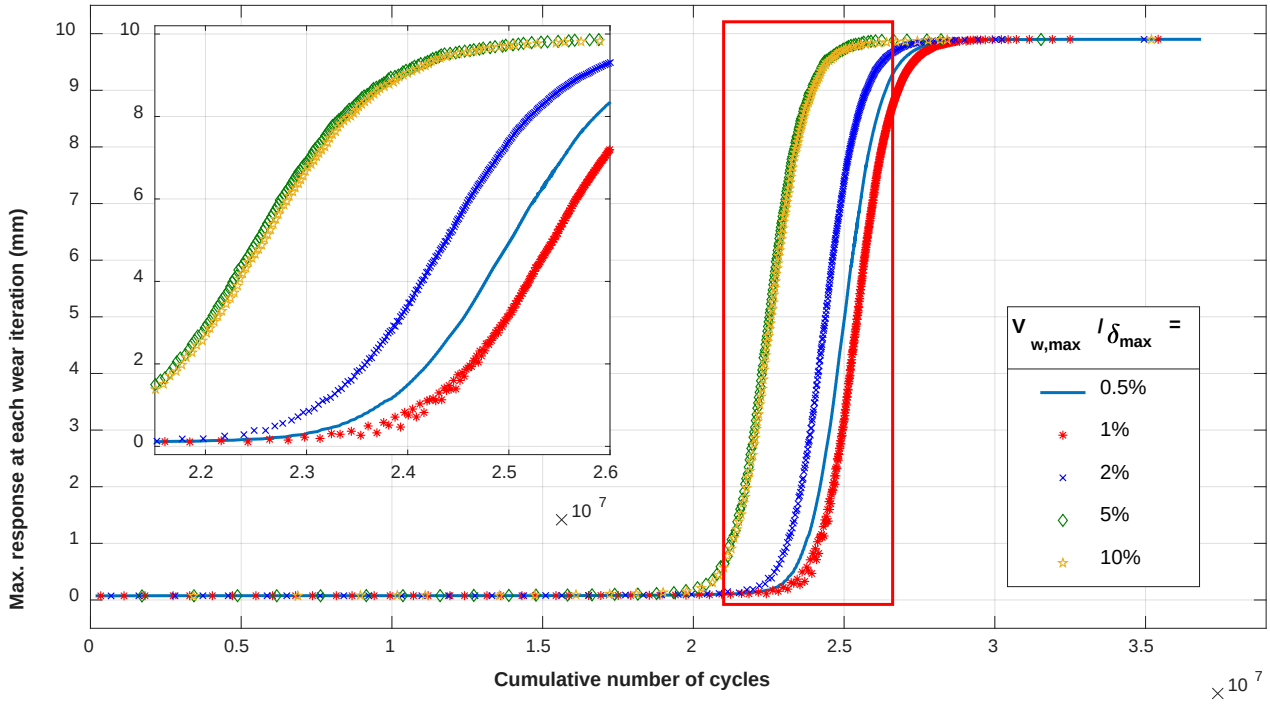

Figure 13: Maximum response at each wear iteration vs the cumulative number of cycles for different values of $\mathbf{v}_{w,max}/\boldsymbol{\delta}_{max}$

Table 2 summarizes the comparison of the effect of the choice of $\mathbf{v}_{w,max}$ on the computational time, the number of wear iterations necessary for the complete loss of contact, maximum wear depth and the relative error in the maximum wear depth taking $\mathbf{v}_{w,max}/\boldsymbol{\delta}_{max}$ = 0.5% as the reference. The trade-off effect of $\mathbf{v}_{w,max}$ is evident by comparing computational time vs error in wear depth.

Table 2: Comparison of the impact of wear analysis with nonlinear dynamic response solver for different values of $\mathbf{v}_{w,max}$

$\frac{\mathbf{v}_{w,max}}{\delta_{max}}$	Computational time	Total no. of wear iterations	Max. total wear depth (mm)	Relative error in wear depth (%)
0.5 %	19 hr 32 min	577	6.3919	-
1 %	16 hr 10 min	411	6.4230	0.49
2 %	10 hr 17 min	291	6.4849	1.45
5 %	6 hr 0 min	183	6.6260	3.66
10 %	3 hr 57 min	130	6.9668	8.99

3.2 Test Case 2: Tuned shrouded bladed disk

A tuned shrouded bladed disk consisting of 40 blades with identical blades is considered, and the fundamental blade sector is as shown in Figure 14 and described in Table 3. This bladed disk is used as a test case to demonstrate the impact of wear on the dynamics with cyclic symmetry property. A fundamental sector consisting of only one blade is assumed with cyclic symmetry boundary conditions to reduce the size of the problem for nonlinear analysis. The disk is assumed to be infinitely rigid and so fixed boundary conditions are applied at the blade root. In this way, the cyclic symmetry only operates through the blade-to-blade coupling at the shrouds. Maximum static deflection (δ_{max}) in this case is computed as the maximum deflection at the shroud contact patch under open condition for the applied static load in such a way to produce a twisting effect of the blade.

Table 3: Parameters for the shrouded bladed disk and the contact patch

Parameter	**Value**
Material	Steel
Young's modulus (E)	210 GPa
Density (ρ)	7860 kg/m^3
Blade geometry	As shown in Figure 14

Number of blades	40
Contact patch dimension	20mm x 30mm
Contact elements	20 on the left and 20 on the right shroud
Tangential contact stiffness (k_t)	93 N/μm
Normal contact stiffness (k_n)	113 N/μm
Friction coefficient (μ)	0.5
Wear energy coefficient (α)	2e3 μm^3/J
Static load (F_{static})	60 kN
Static load/Excitation ratio (F_{static}/F_{ex})	12
Choice of $\mathbf{v}_{w,max}$	{0.5%, 1%, 2%, 5%, 10%} of δ_{max}

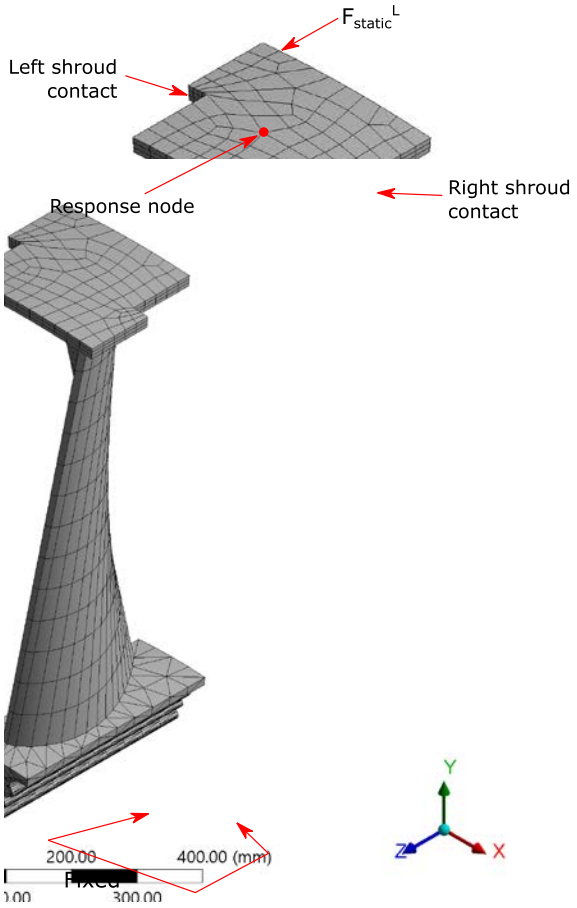

Figure 14: FE model of the blade sector, boundary and loading conditions

Static torque is applied to the blade by two static forces F_{static}, to simulate the twisting effect, actually due to the centrifugal force in rotating blades, which produces the static pre-load at the shrouds. A concentrated

periodic excitation F_{ex} is also applied at a mid-span node of the airfoil. Figure 15(a) highlights the shroud contact patch consisting of 20 contact elements each side with a 5x4 grid. Figure 15(b) shows the typical contact elements distribution between right contact patch with an adjacent blade left contact patch. The friction coefficient, contact stiffnesses and wear energy coefficient is defined as mentioned in Table 3 and are assumed constant throughout the simulation. The nonlinear dynamic analysis is performed by retaining the 0^{th} and the 1^{st} harmonics in the balance equation. First bending mode with first Engine Order (EO = 1) as shown in Figure 16 is chosen as the frequency of interest to analyse the effect of wear on the dynamics of the bladed disk.

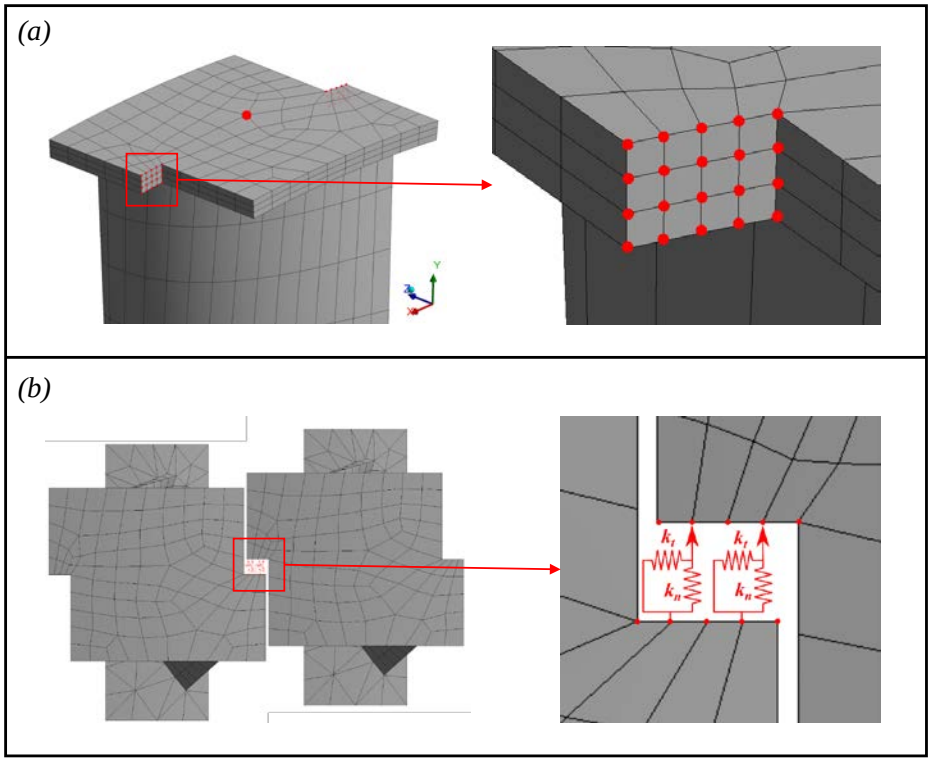

Figure 15: (a) Highlight of the right shroud contact showing 20 contact nodes

(b) Pictorial representation of the applied node-to-node contact model

To define the adaptive wear parameter $\mathbf{v}_{w,max}$, the following logic is applied. The static deflection of the blade is computed under the action of the static forces. Then the average normal displacement of each contact surface is obtained. This value has been set as the maximum possible wear on each surface $\mathbf{v}_{w,max}$, when such a depth is worn out the blades would vibrate freely without any contact with the adjacent blades. Finally, $\mathbf{v}_{w,max}$ is varied from 0.5% to 10% of $\boldsymbol{\delta_{max}}$ in steps indicated in Table 3 to investigate its effect on the accuracy of the model in predicting the evolution of the system dynamics.

Figure 16 shows the nodal diameter versus frequency relationship up to 15 ND for the stuck case. Figure 17 shows the response for various engine order excitations along with the linear free state and stick state curves for the indicated loads.

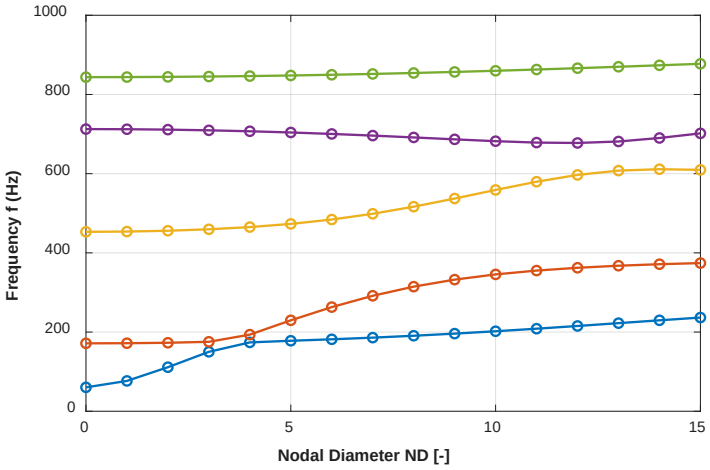

Figure 16: Nodal diameter diagram of the stuck contact shrouded blade

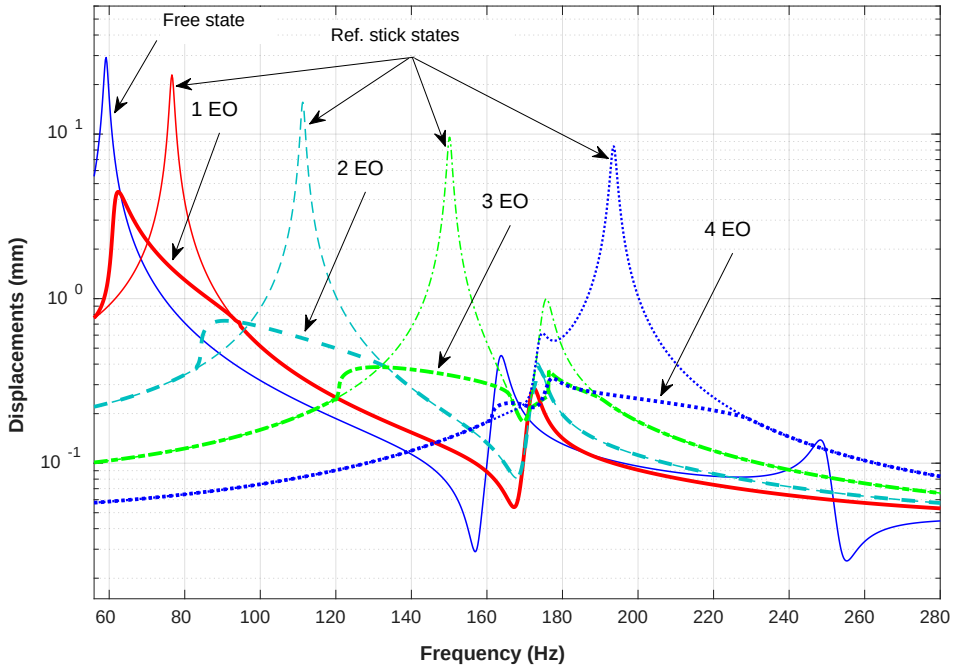

Figure 17: Response to various EO excitations with reference linear free and stick state peaks

Figure 18 shows the nonlinear FRF for the given excitation forces with fixed static load and varying excitation loads. The figure also includes a reference linear free state and stick state for comparison. With the increasing excitation force, the resonance frequency moves towards the free state as the contact nodes experience a larger slip.

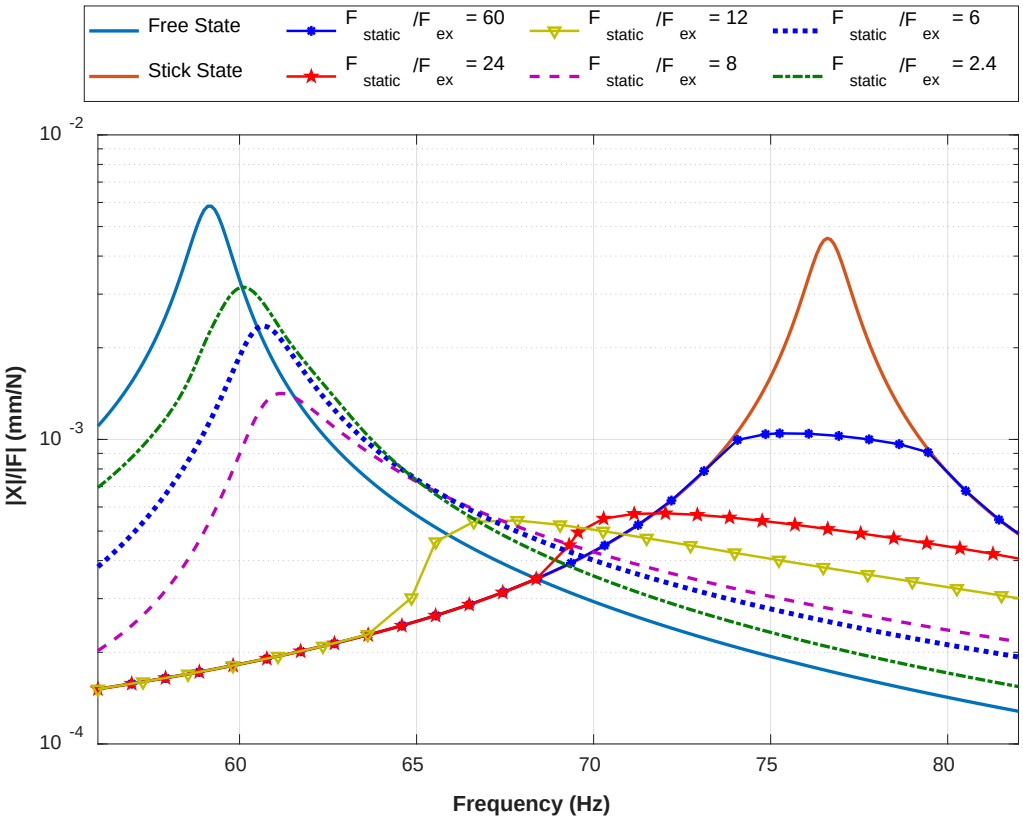

Figure 18: FRF for various excitation loads with a fixed static load (EO = 1)

Figure 19 shows the cumulative wear plot and the contact status plot at various wear iteration intervals. For the given loading conditions, the cumulative wear at the right shroud contact interface, the spatial wear distribution and the contact status at each node can be visualized. At the beginning of the wear, the contact is in the slip-stick state with uniform pressure distribution. As wear progresses, some of the contact nodes are in separation-slip-stick and eventually separation-slip before the complete loss of contact. For simplicity, only one loading condition is shown. The same procedure can be used to visualize various loading conditions and the effect of the adaptive logic parameter $\mathbf{v}_{w,max}$ with an accurate insight at the contact interface behaviour.

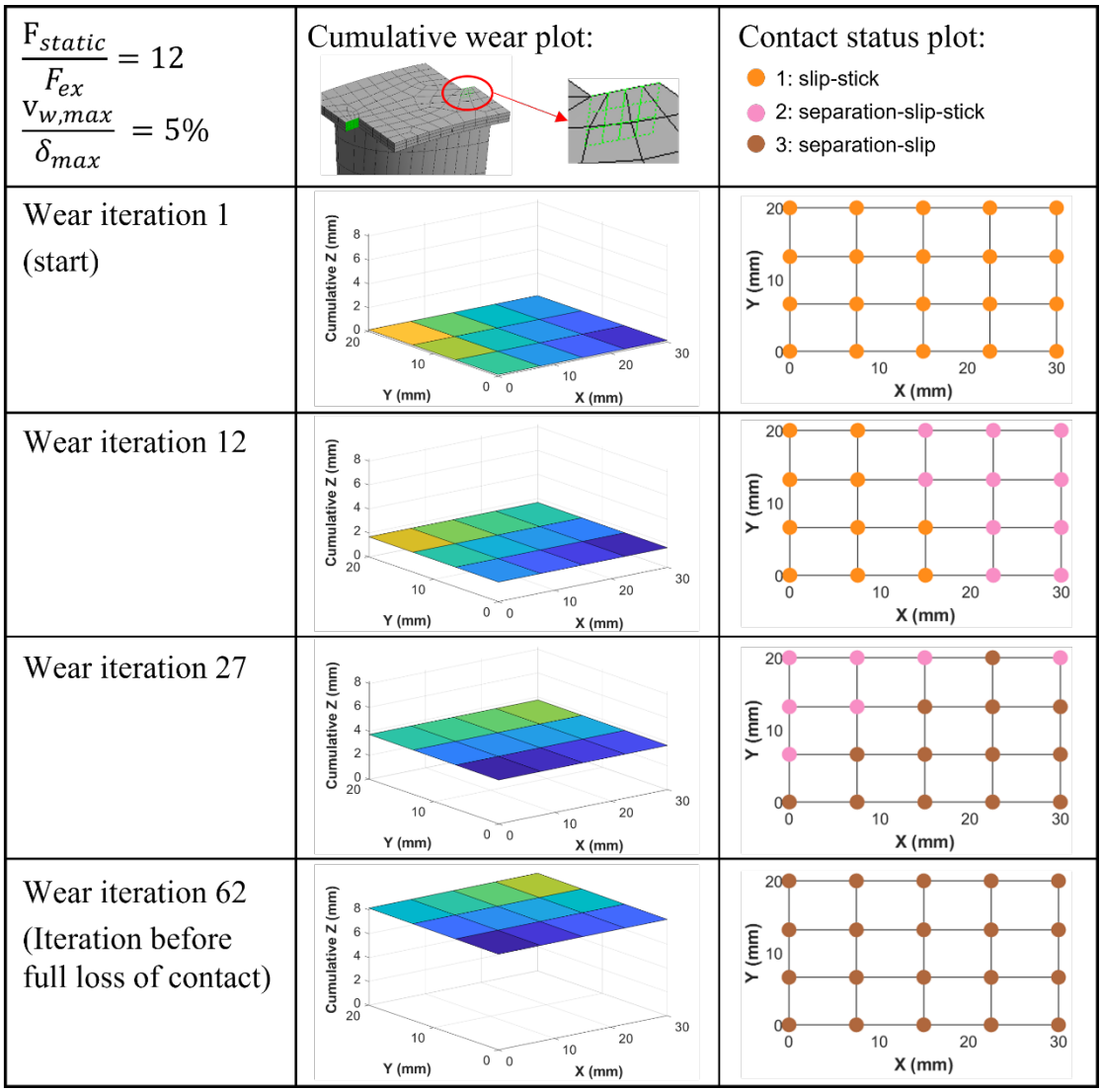

Figure 19: Tabular representation of the cumulative wear plot and contact status plot of the right shroud contact at different wear iterations until the loss of contact for given loading conditions

Figure 20 shows the response with the impact of wear and the backbone of the response curves with the progress of wear. The contact pre-load is continuously changing as the contact is worn and loosens. This loss of contact impacts the dynamic behaviour of the bladed disk. The coupled formulation used in this method is able to effectively update contact pre-load distribution in the nonlinear analysis.

Figure 21 shows the number of wear cycles Z_W at each wear iteration as wear progresses until the loss of contact. It is important to note that the number of cycles at each wear iteration is changing. It is adapted according to the geometry and loading conditions. It is worthy of mentioning that the shape of the curve shown in this figure is not unique. Rather it depends on the loading conditions and the pressure distribution at the contact as well as on the relative contact kinematics at the excited resonance.

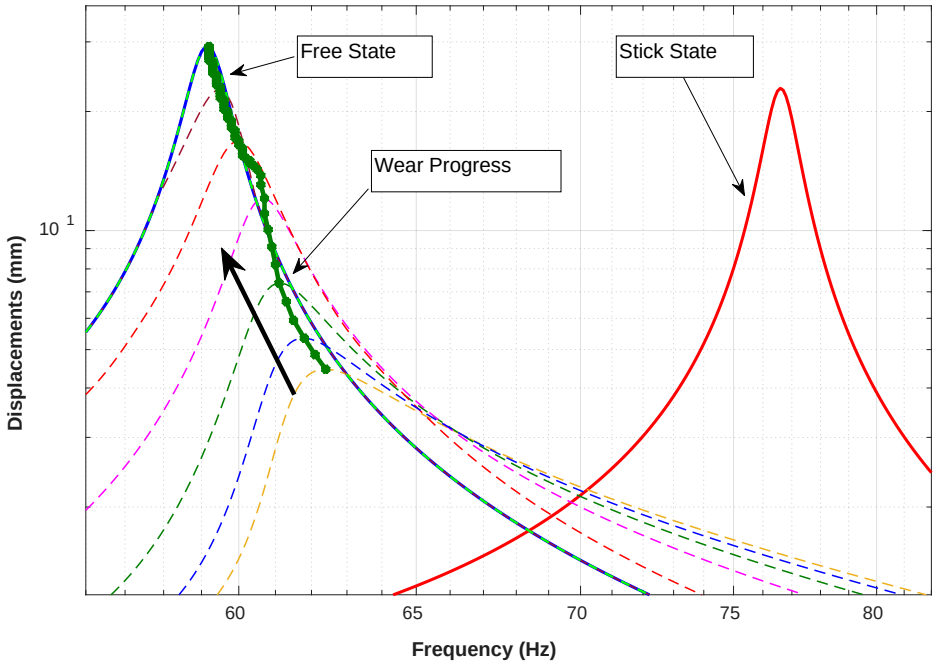

Figure 20: Response graph showing the backbone of the nonlinear response (EO = 1) obtained as wear progresses around first bending mode with free and stick states for reference for $\mathbf{v}_{w,max}$ = 5% of $\boldsymbol{\delta}_{max}$

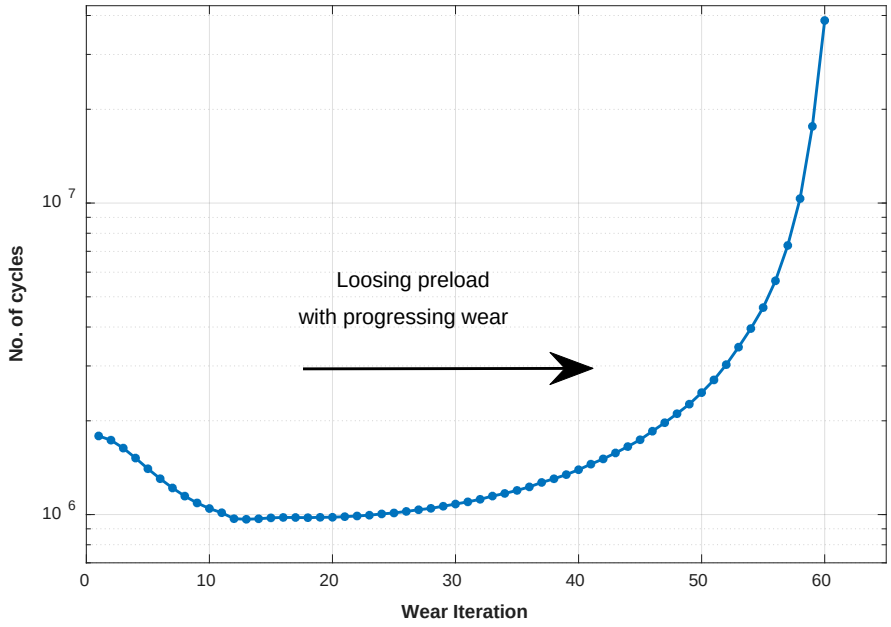

Figure 21: Impact of wear on the number of vibration cycles at each wear iteration until full loss of contact for $\mathbf{v}_{w,max}$= 5% of $\boldsymbol{\delta}_{max}$ [Note: the number of cycles is adaptive at each wear iteration]

It is beneficial to track the maximum response with respect to the cumulative number of cycles as it provides a brief idea of the number of vibration cycles where the amplitude starts to rise considerably. Figure 22 shows

the maximum response versus the cumulative number of cycles until the full loss of contact. Results show that for higher values of $\mathbf{v}_{w,max}$, the rate of change of the response is under-estimated, leading to non-conservative predictions.

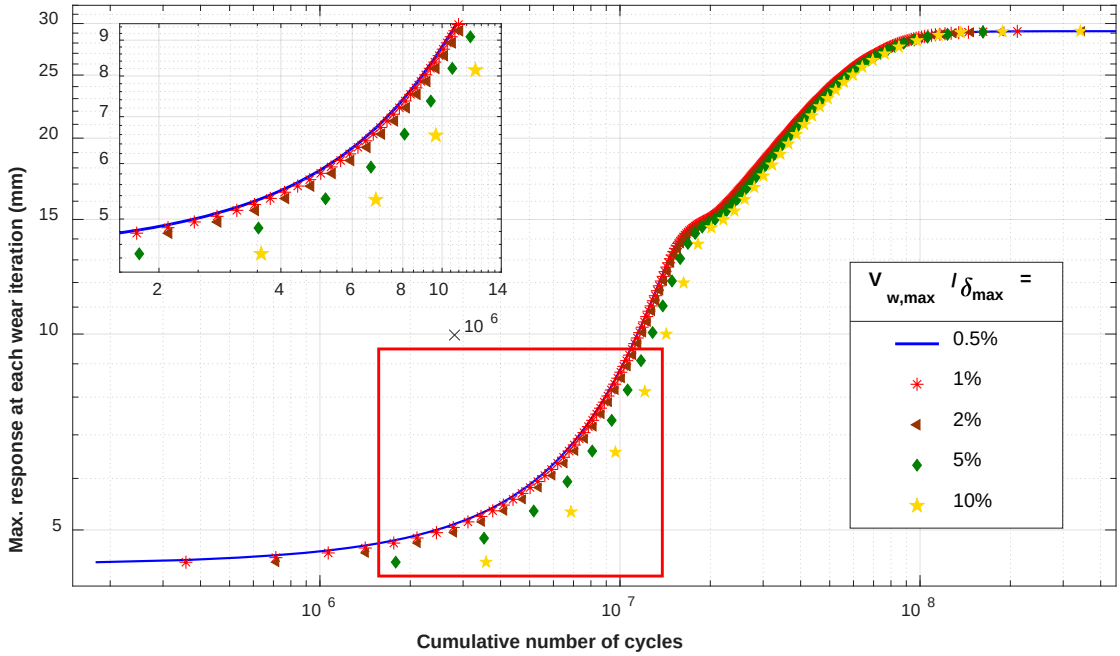

Figure 22: Maximum response at each wear iteration vs the cumulative number of cycles for different values of $\mathbf{v}_{w,max}/\boldsymbol{\delta}_{max}$

Table 4 summarizes the comparison of the effect of the choice of $\mathbf{v}_{w,max}$ on the computational time, number of wear iterations necessary for the complete loss of contact, maximum wear depth and the error in the maximum wear depth.

Table 4: Comparison of the impact of wear analysis with nonlinear dynamic response solver for different values of $\mathbf{v}_{w,max}/\boldsymbol{\delta}_{max}$

$\frac{\mathbf{v}_{w,max}}{\delta_{max}}$	Computational time	Total no. of wear iterations	Max. total wear depth (mm)	Relative error in wear depth (%)
0.5 %	5 hr 17 min	596	8.2566	-
1 %	2 hr 38 min	298	8.2572	0.01
2 %	1 hr 19 min	152	8.2916	0.4

5 %	0 hr 35 min	63	8.3808	1.5
10 %	0 hr 17 min	34	8.4697	2.6

The indicated computational times in Table 2 and Table 4 is the wall clock time obtained when the nonlinear analysis was run on Intel Xeon 4 core processor @ 3.50 GHz and 32 GB RAM standalone workstation.

4. Conclusions

In this paper a novel method to study the effect of wear on the nonlinear dynamics of shrouded blades has been presented. The proposed method is not limited to shrouded blades, but it can be applied to any structures with contact interfaces subjected to wear.

The proposed method is based on the integration of a wear energy model inside a coupled static/dynamic approach suitable for the calculation of the forced response of the system with the HBM. Thanks to the proposed method, wear is directly entered as an input parameter in the contact model, used to compute the periodic contact forces, thus allowing to update the amount and the distribution of static pre-load at the contact without the need for a separate nonlinear static analysis, as in the existing literature.

Also, in order to reduce the calculation time, an adaptive wear acceleration logic is implemented to account for the different time scales typical of wear evolution and vibration. The effect of the choice of a wear acceleration parameter, called $\mathbf{v}_{w,max}$, is investigated. It was shown that with smaller values of $\mathbf{v}_{w,max}$, the change in frequency and amplitude of response curves, wear evolution, and the contact profile is smoother, at the cost of an increased computation time and a higher number of wear iterations. In case of larger values of $\mathbf{v}_{w,max}$, the results are coarse but are obtained with shorter computation times. The choice of $\mathbf{v}_{w,max}$ is a trade-off between the computation time and the accuracy of results.

Acknowledgements

This project has received funding from the European Union's Horizon 2020 research and innovation programme under the Marie Sklodowska-Curie grant agreement No 721865.

References

[1] C. M. Firrone and I. Bertino, “Experimental Investigation on the Damping Effectiveness of Blade Root Joints,” *Experimental Mechanics 2015 55:5*, vol. 55, no. 5, pp. 981–988, Mar. 2015, doi: 10.1007/S11340-015-0001-9.

[2] D. Laxalde, F. Thouverez, and J. P. Lombard, “Forced response analysis of integrally bladed disks with friction ring dampers,” *Journal of Vibration and Acoustics, Transactions of the ASME*, vol. 132, no. 1, pp. 0110131–0110139, Feb. 2010, doi: 10.1115/1.4000763/471095.

[3] K. Y. Sanliturk, D. J. Ewins, and A. B. Stanbridge, “Underplatform Dampers for Turbine Blades: Theoretical Modeling, Analysis, and Comparison With Experimental Data,” *Journal of Engineering for Gas Turbines and Power*, vol. 123, no. 4, pp. 919–929, Oct. 2001, doi: 10.1115/1.1385830.

[4] W. Sextro, “The Calculation of the Forced Response of Shrouded Blades With Friction Contacts and its Experimental Verification,” *Proceedings of the ASME Turbo Expo*, vol. 4, Aug. 2014, doi: 10.1115/2000-GT-0540.

[5] S. Filippi, A. Akay, and M. M. Gola, “Measurement of Tangential Contact Hysteresis During Microslip,” *Journal of Tribology*, vol. 126, no. 3, pp. 482–489, Jul. 2004, doi: 10.1115/1.1692030.

[6] R. B. Waterhouse, “Fretting wear,” *Wear*, vol. 100, no. 1–3, pp. 107–118, 1984, doi: 10.1016/0043-1648(84)90008-5.

[7] J. F. Archard, “Contact and rubbing of flat surfaces,” *Journal of Applied Physics*, vol. 24, no. 8, pp. 981–988, 1953, doi: 10.1063/1.1721448.

[8] G. K. Sfantos and M. H. Aliabadi, “Application of BEM and optimization technique to wear problems,” *International Journal of Solids and Structures*, vol. 43, no. 11–12, pp. 3626–3642, 2006, doi: 10.1016/j.ijsolstr.2005.09.004.

[9] G. K. Sfantos and M. H. Aliabadi, “Wear simulation using an incremental sliding Boundary Element Method,” *Wear*, vol. 260, no. 9–10, pp. 1119–1128, 2006, doi: 10.1016/j.wear.2005.07.020.

[10] P. Arnaud, S. Fouvry, and S. Garcin, “A numerical simulation of fretting wear profile taking account of the evolution of third body layer,” *Wear*, vol. 376–377, pp. 1475–1488, 2017, doi: 10.1016/j.wear.2017.01.063.

[11] S. Fouvry, P. Duó, and P. Perruchaut, “A quantitative approach of Ti-6Al-4V fretting damage: Friction, wear and crack nucleation,” *Wear*, vol. 257, no. 9–10, pp. 916–929, 2004, doi: 10.1016/j.wear.2004.05.011.

[12] S. Toumi, S. Fouvry, and M. Salvia, “Prediction of sliding speed and normal force effects on friction and wear rate evolution in a dry oscillating-fretting PTFE Ti-6Al-4V contact,” *Wear*, vol. 376–377, pp. 1365–1378, 2017, doi: 10.1016/j.wear.2017.02.021.

[13] A. I. Vakis *et al.*, “Modeling and simulation in tribology across scales: An overview,” *Tribology International*, vol. 125, pp. 169–199, 2018, doi: 10.1016/j.triboint.2018.02.005.

[14] L. Gallego, D. Nélias, and C. Jacq, “A Comprehensive Method to Predict Wear and to Define the Optimum Geometry of Fretting Surfaces,” *Journal of Tribology*, vol. 128, no. 3, p. 476, 2006, doi: 10.1115/1.2194917.

[15] A. Fantetti *et al.*, “The Impact of Fretting Wear on Structural Dynamics: Experiment and Simulation,” *Tribology International*, vol. 138, pp. 111–124, 2019, doi: 10.1016/j.triboint.2019.05.023.

[16] R. Lacayo *et al.*, “Nonlinear modeling of structures with bolted joints: A comparison of two approaches based on a time-domain and frequency-domain solver,” *Mechanical Systems and Signal Processing*, 2019, doi: 10.1016/j.ymssp.2018.05.033.

[17] N. M. Newmark, “Newmark A Method of Computation for Structural Dynamics,” 1959. doi: 0.1016/j.compgeo.2015.08.008.

[18] S. Zucca, “Modelling Friction Contacts in Structural Dynamics and its Application to Turbine Bladed Disks”, doi: http://dx.doi.org/10.5772/intechopen.68547.

[19] S. Zucca, C. M. Firrone, and C. Gastaldi, “Models and Methods for the Dynamics of Mechanical Components With Contact Interfaces”.

[20] C. M. Firrone and S. Zucca, “Effect of static/dynamic coupling on the forced response of turbine bladed disks with underplatform dampers,” *Power*, pp. 1–12, 2009, doi: 10.1115/GT2009-59905.

[21] L. Pesaresi, J. Armand, C. W. Schwingshackl, L. Salles, and C. Wong, “An advanced underplatform damper modelling approach based on a microslip contact model,” *Journal of Sound and Vibration*, vol. 436, pp. 327–340, 2018, doi: 10.1016/j.jsv.2018.08.014.

[22] C. Siewert, L. Panning, J. Wallaschek, and C. Richter, “Multiharmonic Forced Response Analysis of a Turbine Blading Coupled by Nonlinear Contact Forces,” *Journal of Engineering for Gas Turbines and Power*, vol. 132, no. 8, p. 082501, 2010, doi: 10.1115/1.4000266.

[23] C. Gastaldi, A. Fantetti, and T. Berruti, “Forced Response Prediction of Turbine Blades with Flexible Dampers: The Impact of Engineering Modelling Choices,” *Applied Sciences*, 2017, doi: 10.3390/app8010034.

[24] S. Nacivet, C. Pierre, F. Thouverez, and L. Jezequel, “A dynamic Lagrangian frequency-time method for the vibration of dry-friction-damped systems,” *Journal of Sound and Vibration*, vol. 265, no. 1, pp. 201–219, 2003, doi: 10.1016/S0022-460X(02)01447-5.

[25] M. Krack and J. Gross, *Harmonic Balance for Nonlinear Vibration Problems*. 2019. doi: 10.1007/978-3-030-14023-6.

[26] M. R. W. Brake, *The Mechanics of Jointed Structures*. 2018. doi: 10.1007/978-3-319-56818-8.

[27] J. Armand, L. Pesaresi, L. Salles, and C. W. Schwingshackl, “A Multiscale Approach for Nonlinear Dynamic Response Predictions with Fretting Wear,” *Journal of Engineering for Gas Turbines and Power*, vol. 139, no. 2, pp. 1–7, 2017, doi: 10.1115/1.4034344.

[28] J. Armand, “Nonlinear dynamics of jointed structures : a multiscale approach to predict fretting wear and its effects on the dynamic response,” 2017.

[29] J. Armand, L. Salles, C. W. Schwingshackl, D. Süß, and K. Willner, “On the effects of roughness on the nonlinear dynamics of a bolted joint: A multiscale analysis,” *European Journal of Mechanics, A/Solids*, vol. 70, no. February, pp. 44–57, 2018, doi: 10.1016/j.euromechsol.2018.01.005.

[30] L. Salles, L. Blanc, A. Gouskov, P. Jean, and F. Thouverez, “Dual Time Stepping Algorithms With the High Order Harmonic Balance Method for Contact Interfaces With Fretting-Wear,” *Journal of Engineering for Gas Turbines and Power*, vol. 134, no. 4, p. 032503, 2011, doi: 10.1115/1.4004236.

[31] L. Salles, A. M. Gouskov, L. Blanc, F. Thouverez, and P. Jean, “Dynamic analysis of fretting-wear in joint interface by a multiscale harmonic balance method coupled with explicit or implicit integration schemes,” *ASME. Turbo Expo: Power for Land, Sea, and Air, Volume 6: Structures and Dynamics, Parts A and B*, vol. 6, pp. 1003–1013, 2010.

[32] L. Salles, L. Blanc, F. Thouverez, A. M. Gouskov, and P. Jean, “Dynamic Analysis of a Bladed Disk With Friction and Fretting-Wear in Blade Attachments,” *Proceedings of ASME Turbo Expo 2009: Power for Land, Sea and Air*, pp. 465–476, 2009, doi: 10.1115/GT2009-60151.

[33] L. R. Tamatam, D. Botto, and S. Zucca, “Effect of wear on the dynamics of structures with contact interfaces by a coupled static/dynamic multi-harmonic balance method,” in *First International Nonlinear Dynamics Conference. Book of abstracts*, 2019, no. 1, pp. 129–130.

[34] L. R. Tamatam, D. Botto, and S. Zucca, “A coupled approach to model the effect of wear on the dynamics of bladed disks,” in *Internation congress on sound and vibration (ICSV26)*, 2019, pp. 1–8.

[35] C. M. Firrone, S. Zucca, and M. M. Gola, “The effect of underplatform dampers on the forced response of bladed disks by a coupled static/dynamic harmonic balance method,” *International Journal of Non-Linear Mechanics*, vol. 46, no. 2, pp. 363–375, 2011, doi: 10.1016/j.ijnonlinmec.2010.10.001.

[36] S. Zucca and C. M. Firrone, “Nonlinear dynamics of mechanical systems with friction contacts: Coupled static and dynamic Multi-Harmonic Balance Method and multiple solutions,” *Journal of Sound and Vibration*, vol. 333, no. 3, pp. 916–926, 2014, doi: 10.1016/j.jsv.2013.09.032.

[37] L. Pesaresi, L. Salles, A. Jones, J. S. Green, and C. W. Schwingshackl, “Modelling the nonlinear behaviour of an underplatform damper test rig for turbine applications,” *Mechanical Systems and Signal Processing*, vol. 85, pp. 662–679, Feb. 2017, doi: 10.1016/J.YMSSP.2016.09.007.

[38] M. Z. Huq and J. P. Celis, “Expressing wear rate in sliding contacts based on dissipated energy,” *Wear*, 2002, doi: 10.1016/S0043-1648(01)00867-5.

[39] M. C. C. BAMPTON and R. R. CRAIG, JR., “Coupling of substructures for dynamic analyses.,” *AIAA Journal*, vol. 6, no. 7, pp. 1313–1319, 1968, doi: 10.2514/3.4741.

[40] E. P. Petrov, “A Method for Use of Cyclic Symmetry Properties in Analysis of Nonlinear Multiharmonic Vibrations of Bladed Disks,” *Journal of Turbomachinery*, vol. 126, no. 1, p. 175, 2004, doi: 10.1115/1.1644558.

[41] S. Mehrdad Pourkiaee and S. Zucca, “A Reduced Order Model for Nonlinear Dynamics of Mistuned Bladed Disks with Shroud Friction Contacts,” *Journal of Engineering for Gas Turbines and Power*, vol. 141, no. 1, Jan. 2019, doi: 10.1115/1.4041653.

[42] G. Jenkins, “Analysis of the stress-strain relationships in reactor grade graphite,” *British Journal of Applied Physics*, vol. 13, no. 1, pp. 30–32, 1962, doi: 10.1088/0508-3443/13/1/307.

[43] W. D. Iwan, “A Distributed-Element Model for Hysteresis and Its Steady-State Dynamic Response,” *Journal of Applied Mechanics*, vol. 33, no. 4, pp. 893–900, 1966, doi: 10.1115/1.3625199.

[44] K. Valanis, *Fundamental Consequences of a New Intrinsic Time Measure. Plasticity as a Limit of the Endochronic Theory*, vol. 32. 1978.

[45] J. H. Griffin, “Friction Damping of Resonant Stresses in Gas Turbine Engine Airfoils,” *Journal of Engineering for Power*, vol. 102, no. 2, pp. 329–333, 1980, doi: 10.1115/1.3230256.

[46] C.-H. Menq, J. Bielak, and J. H. Griffin, “The influence of microslip on vibratory response, part I: A new microslip model,” *Journal of Sound and Vibration*, vol. 107, no. 2, pp. 279–293, Jun. 1986, doi: 10.1016/0022-460X(86)90238-5.

[47] C. C. de Wit, H. Olsson, K. J. Astrom, and P. Lischinsky, “A new model for control of systems with friction,” *IEEE Transactions on Automatic Control*, vol. 40, no. 3, pp. 419–425, 1995, doi: 10.1109/9.376053.

[48] B. D. Yang and C. H. Menq, “Characterization of 3D Contact Kinematics and Prediction of Resonant Response of Structures Having 3D Frictional Constraint,” *Journal of Sound and Vibration*, vol. 217, no. 5, pp. 909–925, 1998.

[49] D. J. Segalman, “A Four-Parameter Iwan Model for Lap-Type Joints,” *Journal of Applied Mechanics*, vol. 72, no. 5, pp. 752–760, 2005, doi: 10.1115/1.1989354.

[50] M. Brake, “A reduced Iwan model that includes pinning for bolted joint mechanics,” *Nonlinear Dynamics*, vol. 87, no. 2, pp. 1335–1349, 2017, doi: 10.1007/s11071-016-3117-2.

[51] R. Bouc, “A Mathematical Model for Hysteresis,” *Acustica*, vol. 24, no. 1, pp. 16–25, 1971.

[52] Y.-K. Wen, “Method for Random Vibration of Vibrating System,” *Nanotechnology*, vol. 8287, pp. 142–145, 1976, doi: 10.1002/mop.

[53] K. Y. Sanliturk and D. J. Ewins, “Modelling Two-Dimensional Friction Contact and Its Application Using Harmonic Balance Method,” *Journal of Sound and Vibration*, vol. 193, no. 2, pp. 511–523, 1996, doi: 10.1006/jsvi.1996.0299.

[54] E. P. Petrov and D. J. Ewins, “Analytical Formulation of Friction Interface Elements for Analysis of Nonlinear Multi-Harmonic Vibrations of Bladed Disks,” *Journal of Turbomachinery*, vol. 125, no. 2, p. 364, 2003, doi: 10.1115/1.1539868.

[55] T. M. Cameron and J. H. Griffin, “An Alternating Frequency / Time Domain Method for Calculating the Steady-State Response of Nonlinear Dynamic Systems,” *Journal of Applied Mechanics*, vol. 56, p. 149, 1989, doi: http://dx.doi.org/10.1115/1.3176036.

[56] O. Poudou and C. Pierre, “Hybrid Frequency-Time Domain Methods for the Analysis of Complex Structural Systems with Dry Friction Damping,” *44th AIAA/ASME/ASCE/AHS/ASC Structures, Structural Dynamics, and Materials Conference*, no. April, pp. 1–14, 2003, doi: 10.2514/6.2003-1411.

[57] A. Cardona, A. Lerusse, and M. Géradin, “Fast Fourier nonlinear vibration analysis,” *Computational Mechanics*, vol. 22, no. 2, pp. 128–142, 1998, doi: 10.1007/s004660050347.

[58] M. Allara, “A model for the characterization of friction contacts in turbine blades,” *Journal of Sound and Vibration*, vol. 320, no. 3, pp. 527–544, 2009, doi: 10.1016/j.jsv.2008.08.016.

[59] M. Ciavarella, D. A. Hills, and G. Monno, “The influence of rounded edges on indentation by a flat punch,” *Proceedings of the Institution of Mechanical Engineers, Part C: Journal of Mechanical Engineering Science*, vol. 212, no. 4, pp. 319–327, 1998, doi: 10.1243/0954406981521259.

[60] J. C. Jäger, “A new principle in contact mechanics,” *ASME J Tribology*, vol. 120, no. October 1998, pp. 677–684, 1998, doi: 10.1115/1.2833765.

[61] K. L. Johnson, *Contact Mechanics*. Cambridge: Cambridge University Press, 1985. doi: 10.1017/CBO9781139171731.

[62] H. C. Meng and K. C. Ludema, “Wear models and predictive equations: their form and content,” pp. 443–457, 1995.

[63] S. Fouvry, T. Liskiewicz, P. Kapsa, S. Hannel, and E. Sauger, “An energy description of wear mechanisms and its applications to oscillating sliding contacts,” *Wear*, 2003, doi: 10.1016/S0043-1648(03)00117-0.

[64] D. Botto and M. Lavella, “High temperature tribological study of cobalt-based coatings reinforced with different percentages of alumina,” *Wear*, vol. 318, no. 1–2, pp. 89–97, 2014, doi: 10.1016/j.wear.2014.06.024.

[65] M. Lavella and D. Botto, “Fretting wear characterization by point contact of nickel superalloy interfaces,” *Wear*, vol. 271, no. 9–10, pp. 1543–1551, 2011, doi: 10.1016/j.wear.2011.01.064.

[66] D. Botto and M. Umer, “A novel test rig to investigate under-platform damper dynamics,” *Mechanical Systems and Signal Processing*, vol. 100, pp. 344–359, 2018, doi: 10.1016/j.ymssp.2017.07.046.